

Cavity–polariton dispersion and polarization splitting in single and coupled semiconductor microcavities

© Giovanna Panzarini, Lucio Claudio Andreani, A. Armitage*, D. Baxter*, M.S. Skolnick*, V.N. Astratov*, J.S. Roberts*, Alexey V. Kavokin**, Maria R. Vladimirova**, M.A. Kaliteevski***

Istituto Nazionale per la Fisica della Materia–Dipartimento di Fisica "A. Volta", Università di Pavia, via Bassi 6, 27100 Pavia, Italy

* Department of Physics, University of Sheffield, Sheffield S3 7RH, United Kingdom

** LASMEA, Université Blaise Pascal Clermont II, Complexe Scientifique des Cézeaux, 24, Avenue des Landais, 63177 Aubiere Cedex, France

*** A.F. Ioffe Physico-technical Institute of The Russian Academy of Sciences, 194021 St.Petersburg, Russia

(February 9, 1999)

Recent theoretical and experimental work on linear exciton-light coupling in single and coupled semiconductor microcavities is reviewed: emphasis is given to angular dispersion and polarization effects in the strong-coupling regime, where cavity-polariton states are formed. The theoretical formulation is based on semiclassical theory. The energy of single-cavity modes is determined by the bare Fabry–Pérot frequency ω_c as well as by the center of the stop band ω_s of the dielectric mirrors; the phase delay in the dielectric mirrors carries a nontrivial angle- and polarization dependence. The polarization splitting of cavity modes depends on the mismatch between ω_c and ω_s , and increases with internal angle as $\sin^2 \theta_{\text{eff}}$. Interaction between the cavity mode and quantum well (QW) excitons is described at each angle by a two-oscillator model, whose parameters are expressed in terms of microscopic quantities. Weak and strong coupling regimes and the formation of cavity polaritons are described. Comparison with experimental results on a GaAs-based cavity with $\text{In}_{0.13}\text{Ga}_{0.87}\text{As}$ QWs shows that a quantitative understanding of polariton dispersion and polarization splitting has been achieved. Coupling of two identical cavities through a central dielectric mirror induces an optical splitting between symmetric and antisymmetric modes. When QW excitons are embedded in both cavities at antinode positions, the system behaves as four coupled oscillators, leading to a splitting of otherwise degenerate exciton states and to separate anticrossing of symmetric and antisymmetric modes. These features are confirmed by experimental results on coupled GaAs cavities with $\text{In}_{0.06}\text{Ga}_{0.94}\text{As}$ QWs. An analysis of reflectivity lineshapes requires the inclusion of the effect of resonance narrowing of cavity polaritons. Finally, the polarization splitting in a coupled cavity depends both on the single-cavity factors and on the angle- and polarization dependence of the optical coupling between the cavities. Inclusion of all these effects provides a good description of the experimental findings.

1. Introduction

The physics of quantum well excitons embedded in semiconductor microcavities is characterized by two regimes. In the weak-coupling case the decay rate and emission pattern of the exciton may be modified, but a radiative decay still occurs; in the strong-coupling regime, instead, a reversible energy exchange between exciton and cavity mode takes place. This is related to the formation of mixed exciton-photon states, usually termed cavity polaritons, since they are the analog of the (quasi-) stationary exciton-polariton states occurring in bulk semiconductors [1].

The strong-coupling regime of quantum well (QW) excitons in microcavities (MCs) is a peculiar and interesting phenomenon, which allows cavity quantum electrodynamic effects to be studied in a solid-state environment, and which has been the subject of numerous investigations in recent years. After the pioneering observation of a Rabi (polariton) splitting in III–V Fabry–Pérot MCs [2], important developments have been the measurement of the polariton dispersion by angle-resolved photoluminescence [3], demonstration of a Rabi

splitting at room temperature [4] and of Rabi oscillations in real time [5], tuning of the exciton-cavity coupling by electric [6] and magnetic [7–10] fields or temperature [6], saturation and bleaching effects [11], studies of relaxation and time-resolved photoluminescence [12–15], effects of disorder and motional narrowing [16–22]. Crossover from polariton doublet to Mollow triplet under high excitation has been demonstrated [23]. Larger Rabi splittings have been observed in II–VI microcavities [24,25], where stimulation effects have also been reported [25], and in organic microcavities [26,27]. Reviews of these and related topics, as well as of semiclassical and quantum treatments, can be found in [28–30].

Recently the system of two coupled MCs with embedded QWs has also been investigated [31–33], as a way to further increase the flexibility in controlling both radiation and material degrees of freedom. In particular, coupled MCs allow a sizeable and measurable radiative splitting of excitons in QWs separated by a macroscopic distance ($> 2\ \mu\text{m}$) to be achieved [33]. A radiative splitting between excitons in electronically uncoupled QWs exists in principle also for QWs without MCs [34] or in a single cavity [35], but in

this case the effect is very small and easily washed out by disorder. Coupled cavities made of porous silicon have also been studied [36]. Angle- and polarization resolved reflectivity experiments on coupled cavities yield detailed information on exciton-photon interactions, which call for accurate yet sufficiently simple theoretical treatments.

A basic piece of information for all the above-mentioned studies is a precise knowledge of polariton dispersion for MCs containing QW excitons. A difficulty which must be faced by a theoretical treatment is to give a realistic description of the phase delay and penetration depth of light in the dielectric mirrors. A derivation of the phase delay [37] and of an accurate secular equation for mixed cavity modes in single cavities [38] have been given previously only for normal incidence. In extending these treatments to oblique incidence, the different polarizations of light (transverse electric, TE, and transverse magnetic, TM) must be considered. Theoretically, the difference in TE and TM polarized reflectivity spectra of quantum well microcavities was discussed in [39,40]; the only experimental reports of a polarization splitting of cavity polaritons are those of [41,33].

In this paper we present a comprehensive theoretical and experimental study of cavity-polariton dispersion in single and coupled MCs with embedded QWs. By the use of linear semiclassical theory we derive analytic formulas for cavity-mode dispersion and cavity-polariton eigenfrequencies for both TE and TM light polarizations. Angle- and polarization-resolved reflectivity results on single and coupled GaAs cavities with InGaAs QWs are presented and compared with theoretical predictions; in particular, the effect of cavity mismatch and absorption of the intensity of reflectivity features, as well as the different factors which influence the polarization splitting, are studied in detail. A full theoretical analysis of the single-cavity results of [41] is presented, which is found to be in good agreement with the experiment. From a careful analysis of reflectivity results for coupled cavities, evidence of line narrowing of cavity polaritons in the resonance region is obtained.

The rest of this paper is organized as follows. In Sec. 2 we give a brief account of the theoretical framework. In Sec. 3 we derive formulas for reflection phase delay and penetration depth in dielectric mirrors when the frequency is close to the center of the stop band, thereby extending the results of [37] to the case of oblique incidence. In Sec. 4 we study a single cavity and obtain results for the empty-cavity mode, polariton dispersion, and polarization splitting; the role of energy-dependent refractive index in determining the polariton dispersion is emphasized. Experimental results are then presented and compared with theory. In Sec. 5 we treat coupled cavities, and derive analytic formulas for optical splitting of the two modes, empty-cavity dispersion and polariton energies; experimental results on coupled cavities are presented and discussed. Section 6 contains concluding remarks. Some derivations and results of the analytic treatment are given in the Appendices.

2. Theoretical framework

The present treatment is based on the semiclassical theory of exciton-radiation interaction. This approach [42], which consists in solving Maxwell equations together with a constitutive relation between electric and displacement fields, yields the same results as a full quantum mechanical theory as far as linear polariton properties are considered; this follows from the fact that the quantum exciton-radiation Hamiltonian is quadratic in the exciton and photon operators [28].

For a layered system it is useful to formulate Maxwell equations in terms of a transfer matrix approach [43–45]. We take the z -axis to coincide with the growth direction; for any incidence angle and for TE (or s) and TM (or p) polarizations the transfer matrix $T(z_l \rightarrow z_r)$ is a 2×2 matrix which acts on the basis of right- and left-travelling waves and which propagates the electric field from a point z_l to a point z_r in the structure. The transfer matrix is unimodular, when the refractive indices n_l, n_r of left and right media are the same, otherwise $\det(T) = n_l/n_r$. Evaluation of the transfer matrix T of the whole structure — which is simply obtained by multiplying from the left the transfer matrices of the different regions — provides the reflection and transmission coefficients, which in this paper are always considered for light incident from the left:

$$r = -\frac{T_{21}}{T_{22}}, \quad t = \frac{\det(T)}{T_{22}} = \frac{n_l}{n_r} \frac{1}{T_{22}}; \quad (1)$$

the reflectivity R and transmittivity T are then given by

$$R = |r|^2, \quad T = \frac{n_r}{n_l} |t|^2 = \frac{n_l}{n_r} \frac{1}{|T_{22}|^2}. \quad (2)$$

Absorption is given by $A = 1 - R - T$. The poles of the reflection and transmission coefficients, namely the complex frequencies ω which satisfy the equation $T_{22}(\omega) = 0$, give finally the energies and halfwidths of a resonance.

Useful parametrized forms of the transfer matrix can be given for the special cases of a non-absorbing or of a symmetric structure; they are derived by imposing the requirements of invariance under the time-reversal operation, or under specular reflection, respectively. The most general transfer matrix of a non-absorbing structure is expressed as [38]

$$T_{\text{non-abs}} = \frac{n_l}{n_r} \begin{bmatrix} 1/t^* & -r^*/t^* \\ -r/t & 1/t \end{bmatrix} \quad (3)$$

in terms of the reflection and transmission coefficients. The mirror image of the structure has a transfer matrix \tilde{T} given by

$$\tilde{T}_{\text{non-abs}} = \begin{bmatrix} 1/t^* & r/t \\ r^*/t^* & 1/t \end{bmatrix}. \quad (4)$$

If in addition the structure is symmetric, the two matrices T and \tilde{T} are identical, therefore $t/t^* = -r/r^*$. For a general symmetric structure (but which may be absorbing, so that

time reversal is not a good symmetry operation) the transfer matrix can be expressed as [43,44]

$$T_{\text{sym}} = \frac{1}{t} \begin{bmatrix} t^2 - r^2 & r \\ -r & 1 \end{bmatrix}, \quad (5)$$

where again r, t represent the reflection and transmission coefficients from the left side.

We describe each layer in the structure by a local dielectric constant, the only exception being the QW regions. For the QWs we use a nonlocal susceptibility evaluated by linear response theory, which incorporates the microscopic details of the exciton envelope function. The QW transfer matrix at oblique incidence for TE and TM polarizations has the form (5). The difference between TE and TM polarized light appears in reflection and transmission coefficients. These depend on the scattering amplitudes of the e. m. field modes coupled to the exciton polarized along different directions: T -mode (in-plane polarized, transverse), L -mode (in-plane polarized, longitudinal), and Z -mode (polarized along the growth direction) [39,46]. For TE polarization

$$r_{\text{QW}}^{\text{TE}} = -\frac{i\Gamma_T}{\Delta + i\Gamma_T}, \quad t_{\text{QW}}^{\text{TE}} = 1 + r_{\text{QW}}^{\text{TE}}, \quad (6)$$

while for TM polarization

$$r_{\text{QW}}^{\text{TM}} = r_L - r_Z, \quad t_{\text{QW}}^{\text{TM}} = 1 + r_L + r_Z, \quad (7)$$

with

$$r_L = -\frac{i\Gamma_L}{\Delta + i\Gamma_L}, \quad r_Z = -\frac{i\Gamma_Z}{\Delta - \delta_{ZT} + i\Gamma_Z}; \quad (8)$$

the case of TM polarization is more complex since the scattering amplitudes of L - and Z modes interfere. In the above formulas $\Delta = \omega - \omega_{\text{ex}} + i\gamma_{\text{ex}}$ (we neglect the weak dependence of the exciton frequency ω_{ex} on in-plane wavevector and polarization), δ_{ZT} is the splitting between Z and T exciton polaritons in the QW [45], γ_{ex} is the non radiative exciton broadening. A radiative broadening follows from coupling of the QW exciton to the radiation field through Maxwell equations [47–49], and it depends on the angle θ_c in the medium. For the in-plane polarized T and L modes it is given by $\Gamma_T = \Gamma_0 / \cos \theta_c$, $\Gamma_L = \Gamma_0 \cos \theta_c$, where $\Gamma_0 = \frac{\pi}{n_c} \left(\frac{e^2}{4\pi\epsilon_0 mc} \right) f_{xy}$ is the radiative decay rate of the QW exciton amplitude at zero in-plane wavevector (f_{xy} is the oscillator per unit area, m is the free electron mass and ϵ_0 is the vacuum permittivity). Concerning the z -polarized mode, for the heavy hole exciton resonance $\Gamma_Z = 0$, while for the light hole exciton $\Gamma_Z = 4\Gamma_0((\cos \theta_c)^{-1} - \cos \theta_c)$. In the following we will only consider the heavy hole excitons. Substituting the above coefficients r and t into the general transfer matrix (5), for a symmetric structure one can obtain in this case:

$$T_{\text{QW}}^\alpha = \frac{1}{\Delta} \begin{bmatrix} \Delta - i\Gamma^\alpha & -i\Gamma^\alpha \\ i\Gamma^\alpha & \Delta + i\Gamma^\alpha \end{bmatrix}, \quad \alpha = \text{TE, TM}. \quad (9)$$

Here $\Gamma^{\text{(TE)}} \equiv \Gamma_T$, $\Gamma^{\text{(TM)}} \equiv \Gamma_L = \Gamma_T \cos^2 \theta_c$. The angle θ_c in the cavity is related to the external angle θ by $\sin \theta_c = (\sin \theta) / n_c$.

3. Dielectric mirrors

The simplest semiconductor microcavity structure is a planar Fabry–Pérot cavity, bounded by dielectric mirrors termed distributed Bragg reflectors (DBRs) [50–52]. A DBR is a periodic quarter wave stack consisting of alternating layers of high and low refractive index materials, with the optical thickness of each layer a quarter wave at the operating wavelength. The most useful feature of a DBR, which is a consequence of propagation of e. m. waves in periodic layered media, is the existence of a “stop band” region in which radiation cannot propagate; in this frequency region constructive interference between rays reflected from successive periods leads to reflectivity values close to unity. The center of the stop band (denoted by ω_s in this paper) is determined by the $\lambda/4$ condition, whereas the fractional bandwidth depends on the refractive indices n_1 and n_2 of the two materials according to $\Delta\omega_s/\omega_s = (4/\pi) \arcsin(|n_2 - n_1|/(n_2 + n_1))$. A proper treatment of the phase delay on reflection by a DBR is a preliminary issue in order to calculate the angular dispersion of cavity polaritons for TE and TM polarizations. Previous work on angular dependence of phase delay in Fabry–Pérot filters (but neglecting the difference of polarizations) is described in [53].

We consider a DBR with layer thicknesses a, b , and refractive indices n_1, n_2 which can be either in the order $n_1 < n_2$ (as exemplified in Fig. 1) or $n_1 > n_2$; our treatment applies to both situations. First we consider the periodic structure with N periods of Fig. 1, a and calculate its transfer matrix T_N (see e. g. [52]). Then we take a DBR surrounded from the left by a cavity medium with refractive

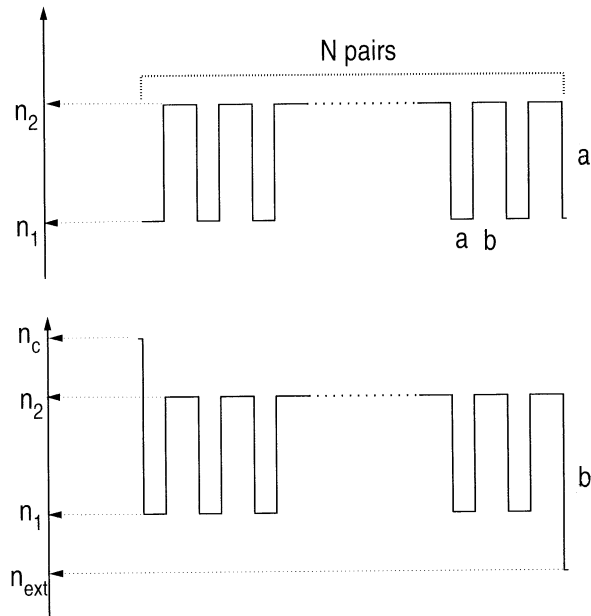


Рис. 1. Refractive index profiles of (a) the periodic DBR structure, and (b) the DBR surrounded on the left by a cavity with refractive index n_c and on the right by an external medium with refractive index n_{ext} .

index n_c and from the right, by an external medium with refractive index n_{ext} (Fig. 1, *b*), which is our structure of interest, and evaluate its transfer matrix by multiplying T_N with appropriate interface matrices. The resulting transfer matrix is expressed in the general form (3) for non-absorbing materials.

We now derive an approximate, parametrized expression for the reflection coefficient of the DBR showing its dependence on angle and polarization. At frequencies close to the center of the stop band $\omega_s^\alpha(\theta)$, $\alpha = \text{TE, TM}$, the reflection coefficient of a DBR at a fixed angle may be assumed to have a constant amplitude and a phase which is linear in $(\omega - \omega_s^\alpha(\theta))$:

$$r_{\text{DBR}}^\alpha(\omega) = \pm \sqrt{R^\alpha} \exp \left[i \frac{n_c}{c} L_{\text{DBR}}^\alpha(\omega - \omega_s^\alpha) \cos \theta_c \right]. \quad (10)$$

The upper (lower) sign holds for $n_1 < n_2$ ($n_1 > n_2$). Thus when $n_1 < n_2$ the phase of the reflection coefficient is zero at the center of the stop band, and the electric field has a maximum at the boundary between cavity and DBR. This case is realized e.g. for a GaAs cavity with AlAs/GaAs Bragg mirrors, in this case we have $n_c = n_2 = n(\text{GaAs})$, $n_1 = n(\text{AlAs})$. In the opposite case $n_1 > n_2$ the phase of the reflection coefficient equals π at the center of the stop band (like for a metallic mirror), and the electric field vanishes at the boundary.

The quantity $L_{\text{DBR}}^\alpha(\theta)$ represents a penetration depth of the field in the dielectric mirror, dependent on both angle

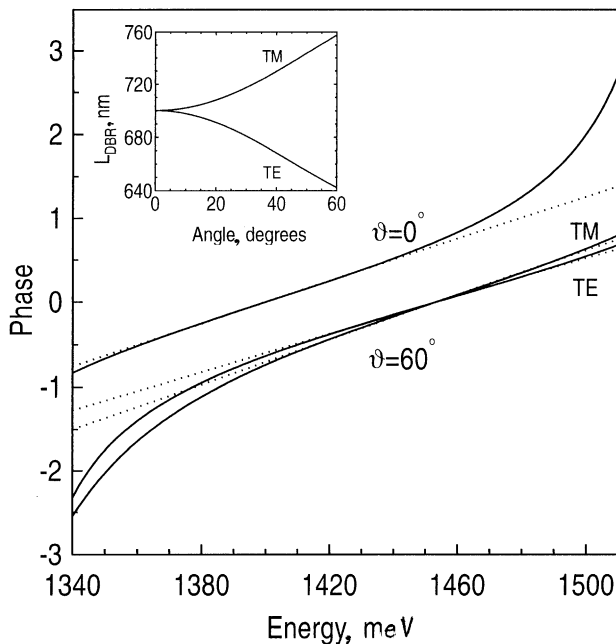


Рис. 2. Phase of the reflection coefficient of a AlAs/GaAs DBR close to the center of the stop band ($\omega_s = 1.4$ eV at normal incidence), at $\theta = 0$ and at $\theta = 60^\circ$ for TE and TM polarizations. Solid lines: numerical simulations with $N = 12$. Dotted lines: analytic formula (see Eq. (10)). Inset: angular dependence of mirror penetration depth for the two polarizations.

and polarization. At normal incidence it equals $2L_\tau$, where L_τ is defined in [37] as the distance at which a fixed-phase mirror has to be displaced in order to produce the same phase delay on reflection. For TE-polarization this kind of parametrization has been used in [40]. Expressions for the parameters $R^\alpha(\theta)$, $L_{\text{DBR}}^\alpha(\theta)$, $\omega_s^\alpha(\theta)$ appearing in Eq. (10) are given in Appendix A.

In Fig. 2 we show the phase of the reflection coefficient of a AlAs/GaAs DBR, calculated with the formulas of Appendix A, compared with the results of a numerical simulation. The parameters are close to those of the experimental results to be shown later. We have assumed the $\lambda/4$ condition to be satisfied at $\hbar\omega_s = 1.4$ eV, with refractive indices $n_1 = 3.01$ for AlAs and $n_2 = 3.55$ for GaAs. We have considered the cases of normal incidence, and of $\theta = 60^\circ$ for TE and TM polarizations. The comparison shows that the assumed linear dependence of the phase of the DBR is a very good approximation in a wide range of frequencies around the center of the stop band. For the chosen parameters the stop band extends from 1.28 to 1.52 eV: the phase of the reflection coefficient varies from $-\pi$ to π in this interval. The inset shows the penetration depth for both polarizations as a function of angle. The penetration depth increases for TM, and decreases for TE polarization; this angular dependence will play an important role in determining the polarization splitting of cavity polaritons.

4. Single microcavity

We consider a symmetric Fabry-Pérot cavity structure of length L_c with a symmetric layer characterized by reflection and transmission coefficients r_c, t_c placed at its center. The transfer matrices of the right and left mirrors are expressed in the forms (3) and (4), respectively, and that of the central structure in the form (5) with $r = r_c$ and $t = t_c$; the transfer matrix T of the whole structure is easily found by multiplying from the left the transfer matrices of the various layers. The eigenmodes are found from the poles of the transmission coefficient (1), i.e., by setting the element T_{22} equal to zero. The equation $T_{22}(\omega) = 0$ for the eigenfrequencies can be put in the following form [39] (with $k_z = (n_c\omega/c) \cos \theta_c$):

$$\left[r_{\text{DBR}}(r_c + t_c) e^{ik_z L_c} \right] \left[r_{\text{DBR}}(r_c - t_c) e^{ik_z L_c} - 1 \right] = 0. \quad (11)$$

This is an equation for the frequency ω in the complex plane. One can easily prove [40] that the first bracket in Eq. (11) is equal to zero at the eigenfrequency of a mode even with respect to the center of the cavity, while the zero of the second bracket corresponds to an odd cavity mode. The above equation is general and applies to several specific situations, e.g. an empty cavity ($r_c = 0, t_c = 1$), a cavity with one quantum well ($r_c = r_{\text{QW}}, t_c = t_{\text{QW}}$), a cavity with two sets of QWs in symmetric positions [35,40], or even a coupled cavity if the central object is another DBR.

4.1. Empty cavity. By specifying Eq. (11) to the case of an empty cavity, the eigenfrequencies of the cavity modes

are determined by the equation $r_{\text{DBR}}^2 \exp(2ik_z L_c) = 1$. By using the parametrization (10) and taking the logarithm, the equation for the complex frequency becomes (for simplicity the polarization index is understood in all subsequent formulas)

$$2 \frac{n_c}{c} \left[L_c \omega + L_{\text{DBR}}(\theta) (\omega - \omega_s(\theta)) \right] \cos \theta_c = 2\pi m + i \ln R, \quad (12)$$

where $R = |r_{\text{DBR}}|^2$ is the mirror reflectivity and the integer m represents the number of half wavelengths contained in the cavity region. The complex frequency is denoted by $\omega_m^\alpha(\theta) - i\gamma_m^\alpha(\theta)$ ($\alpha = \text{TE, TM}$), where ω_m is the real frequency of the mode and γ_m is the mode halfwidth (HWHM); they are determined by the real and imaginary parts of Eq. (12), respectively. The real part of (12) gives the phase-matching condition, and leads to a cavity–mode frequency ω_m which can be expressed in the form

$$\omega_m(\theta) = \frac{L_c \omega_c(\theta) + L_{\text{DBR}}(\theta) \omega_s \theta}{L_{\text{eff}}(\theta)}, \quad (13)$$

where $L_{\text{eff}} = L_c + L_{\text{DBR}}$ is an effective cavity length, and $\omega_c = m\pi c / (n_c L_c \cos \theta_c)$ is the Fabry–Pérot frequency if there is no phase delay in the mirrors. This expression shows that the cavity mode frequency is a weighted average of ω_c and ω_s ; in most cases L_{DBR} is much larger than L_c , so that ω_m is mostly determined by the center of the stop band. This often unappreciated result implies that the frequency of the cavity mode has only a weak dependence on cavity thickness, while it depends more sensitively on the DBR layer thicknesses: this behavior is verified in numerical simulations as well as in experiments. A useful approximate formula for the dependence of mode energy on cavity length L_c is $\delta\omega_m/\omega_m \simeq \delta L_c/L_{\text{eff}}$. The imaginary part of (12) gives the halfwidth in the limit $R \rightarrow 1$, when $\ln R \simeq -(1 - R)$ as

$$\gamma_m(\theta) = \frac{e(1 - R(\theta))}{2n_c L_{\text{eff}}(\theta) \cos \theta_c}. \quad (14)$$

The above results are given in more general form in Appendix B, where the case of an asymmetric cavity is also considered. The main difference in optical properties of an asymmetric compared to a symmetric cavity is that the minima of reflectivity do not reach zero, i. e., reflectivity dips are much less pronounced.

Although the results of Appendix A are valid for any values of the refractive indices, simpler expressions for the cavity mode dispersion can be given for the common case in which n_c, n_1, n_2 are close to each other. Let us denote by n_{eff} the common value of the refractive index: then the center of the stop band is very closely the same for the two polarizations (as seen from the formulas of Appendix A, and also found numerically), and behaves as $\omega_s(\theta) = \pi c / (n_{\text{eff}}(a + b) \cos \theta_{\text{eff}})$, where a, b are the DBR layer thicknesses: it has therefore the

same angular dependence as the Fabry–Pérot frequency $\omega_c(\theta)$. When the cavity-mode frequency at $\theta = 0$ is factorized, this leads to the frequently used dispersion formula $\omega_m(\theta) = \omega_m(0) / \cos \theta_{\text{eff}}$: this formula can also be viewed as a definition for the effective refractive index [51,53–55]. However the definition implicitly assumes that the refractive index is a constant, i. e., independent of energy. When the energy-dependence of the refractive index is taken into account, it is easy to show that the cavity mode dispersion becomes

$$\omega_m(\theta) = \frac{n_{\text{eff}}[\omega_m(0)] \omega_m(0)}{n_{\text{eff}}[\omega_m(\theta)] \cos \theta_{\text{eff}}}. \quad (15)$$

Although the energy dependence of the refractive index is small, it has an important effect on the angular dependence of the cavity-mode and therefore on the polariton dispersion, as will be shown in Sec. 4.3 by the comparison with the experiments.

An approximate formula for the polarization splitting can also be given for the case $n_c \simeq n_1 \simeq n_2$. While ω_s is very nearly the same for both polarizations, the penetration depth L_{DBR} depends markedly on polarization, as it increases with angle for TM and it decreases for TE polarization (see inset of Fig. 2). From Eq. (13) it can be seen that if $\omega_c = \omega_s$, the cavity mode frequency is independent of L_{eff} and thus it depends very little on polarization. Therefore the polarization splitting is controlled by the mismatch between the center of the stop band ω_s and the Fabry–Pérot frequency ω_c . We can exploit the fact that $\omega_s(\theta)$ varies roughly as $1/\cos \theta_{\text{eff}}$, just like $\omega_c(\theta)$, and obtain the approximate form

$$\omega_m^{\text{TM}}(\theta) - \omega_m^{\text{TE}}(\theta) \simeq \frac{L_c (L_{\text{DBR}}^{\text{TM}}(\theta) - L_{\text{DBR}}^{\text{TE}}(\theta))}{L_{\text{eff}}(0)^2} \times \frac{(\omega_s(0) - \omega_c(0))}{\cos \theta_{\text{eff}}}. \quad (16)$$

The penetration depths can be evaluated by means of the formulas in Appendix A. In the limit $n_1 \simeq n_2 \simeq n_c \equiv n_{\text{eff}}$ the following approximate formula is obtained:

$$\omega_m^{\text{TM}}(\theta) - \omega_m^{\text{TE}}(\theta) \simeq \frac{L_c L_{\text{DBR}}(0)}{L_{\text{eff}}(0)^2} \frac{2 \cos \theta_{\text{eff}} \sin^2 \theta_{\text{eff}}}{1 - 2 \sin^2 \theta_{\text{eff}}} \times (\omega_s(0) - \omega_c(0)). \quad (17)$$

This equation (which is valid for both cases $n_1 < n_2$ and $n_1 > n_2$) is somewhat less accurate compared to Eq. (16), but it displays more clearly the angular dependence: basically, the polarization splitting is proportional to $\omega_s(0) - \omega_c(0)$, and it increases with angle like $\sin^2 \theta_{\text{eff}}$. We emphasize that the TM mode can be at higher or lower energy, according to which of $\omega_s(0)$ or $\omega_c(0)$ is higher: the first case is realized when the DBR period $a + b < \lambda/2$, while the second case (TE higher) occurs when $a + b > \lambda/2$.

4.2. Single cavity with quantum wells. We now consider a cavity of width L_c with one QW at

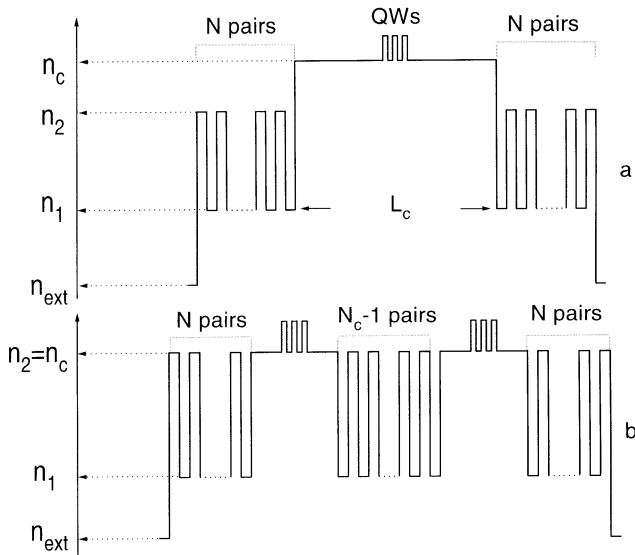


Fig. 3. Refractive index profile of (a) the single cavity structure, and (b) the coupled cavity structure. A set of three QWs at the center of each cavity is indicated.

the center (see Fig. 3, a). The dispersion equations for TE and TM polarized polariton modes can be written in the form of Eq. (11), where r_c, t_c are now the amplitude reflection and transmission coefficients of light from the QW, Eqs. (6), (7). For the heavy-hole exciton $t_{\text{QW}} = 1 + r_{\text{QW}}$, thus in Eq. (11) the vanishing of the second bracket gives simply $r_{\text{DBR}} \exp(ik_z L_c) = -1$: this is equivalent to saying that the QW exciton state (which is symmetric w.r.t. the center of the QW) is not coupled to an antisymmetric cavity mode. The mixed exciton-cavity modes correspond to the symmetric solutions and are described by zeros of the first bracket in Eq. (11), which in the case of the heavy hole exciton resonance reduces to [38]

$$\frac{\Gamma^\alpha}{\omega - \omega_{\text{ex}} + i\gamma_{\text{ex}}} = i \frac{1 - r_{\text{DBR}}^\alpha e^{ik_z L_c}}{1 + r_{\text{DBR}}^\alpha e^{ik_z L_c}}, \quad \alpha = \text{TE, TM}. \quad (18)$$

Far from the frequency of a cavity mode the r.h.s. of (18) is always finite, and the dressed exciton energy can be found by perturbation theory as $\omega = \omega_{\text{ex}} - i\gamma_{\text{ex}} + \Delta\omega_{\text{ex}}$, where the radiative shift $\Delta\omega_{\text{ex}}$ is of the order of the radiative broadening Γ . On the other hand the r.h.s. of (18) vanishes at the frequency of a symmetric cavity mode, and in this case the radiative shift of the exciton cannot be found by perturbation theory: rather, the vanishing of the r.h.s. marks the crossover to a nonperturbative regime of exciton-radiation coupling. The proper way to proceed is to expand the r.h.s. for frequencies close to resonance. We use again the parametrization (10): since the factor $r_{\text{DBR}} \exp(ik_z L_c)$ equals unity at the complex frequency of the cavity mode $\omega_m - i\gamma_m$ (see the discussion leading to Eqs. (12)–(14)), it can be written as $\exp(i \frac{n_c L_c}{c} (\omega - \omega_m + i\gamma_m) \cos \theta_c)$ and the r.h.s. of (18) can be expressed in terms of the (small) difference $\omega - \omega_m + i\gamma_m$. Expanding up to first order in

$(\omega - \omega_m + i\gamma_m)$, the exciton and the cavity mode are found to behave like two coupled, damped oscillators:

$$(\omega - \omega_{\text{ex}} + i\gamma_{\text{ex}})(\omega - \omega_m + i\gamma_m) = V^2, \quad (19)$$

where

$$V^\alpha(\theta) = \left(\frac{2c\Gamma^\alpha(\theta)}{n_c L_{\text{eff}}^\alpha(\theta) \cos \theta_c} \right)^{1/2}, \quad \alpha = \text{TE, TM} \quad (20)$$

is the exciton-cavity coupling depending on angle and polarization. Using the expressions for the angle-dependent radiative widths given in Sec. 1 we have

$$V^{\text{TE}}(\theta) = \left(\frac{1}{4\pi\epsilon_0} \frac{2\pi e^2 f_{xy}}{n_c^2 m L_{\text{eff}}^{\text{TE}}(\theta)} \right)^{1/2} \frac{1}{\cos \theta_c}, \quad (21)$$

$$V^{\text{TM}}(\theta) = \left(\frac{1}{4\pi\epsilon_0} \frac{2\pi e^2 f_{xy}}{n_c^2 m L_{\text{eff}}^{\text{TM}}(\theta)} \right)^{1/2}. \quad (22)$$

Equation (19) is often derived by diagonalizing a 2×2 Hamiltonian, in which two oscillators of frequencies $\omega_{\text{ex}} - i\gamma_{\text{ex}}$ and $\omega_m - i\gamma_m$ are coupled by a matrix element V . The present treatment yields a rigorous derivation of this two-oscillator model, together with microscopic expressions for the various parameters, with their angle- and polarization-dependence.

The occurrence of two distinct regimes is clearly evident when Eq. (19) is solved in the resonant case ($\omega_0 = \omega_m$):

$$\omega = \omega_{\text{ex}} - i \frac{(\gamma_{\text{ex}} + \gamma_m)}{2} \pm \sqrt{V^2 - \frac{1}{4}(\gamma_{\text{ex}} - \gamma_m)^2}. \quad (23)$$

For purely homogeneous broadening as assumed here, the linewidth in the strong-coupling regime is the average of γ_{ex} and γ_m . The weak coupling regime corresponds to an imaginary square root in (23) (i.e., $2V < |\gamma_{\text{ex}} - \gamma_m|$); the exciton decay is still an irreversible process like in an isolated QW, but the emission rate in the direction of the cavity mode may be increased by orders of magnitude [56]. Instead, the strong coupling regime occurs for $2V > |\gamma_{\text{ex}} - \gamma_m|$, and corresponds to a real square root in (23). In this case optical confinement leads not only to a quantitative, but also to a qualitative modification of the emission properties of the system. The eigenmodes are mixed exciton-radiation states and exhibit a splitting in the frequency domain (Rabi splitting) given by

$$\Omega = 2\sqrt{V^2 - \frac{1}{4}(\gamma_{\text{ex}} - \gamma_m)^2}. \quad (24)$$

The maximum value of the splitting occurs when the two linewidths γ_{ex} and γ_m are equal. The frequency splitting corresponds to energy oscillations in the time domain between the exciton and cavity modes.

When N identical QWs are placed in the microcavity, cooperative effects arise. Radiative coupling rearranges the N exciton states into a single, "bright" state which is maximally coupled to light, and $N - 1$ "dark" states which have little interaction with the radiation field [57–60]. The dark states come into play when considering scattering and thermalization of cavity polaritons [14]; also, they can be mixed up with the bright state when disorder is present [60]. Apart from these cases the dark states do not play a role for the optical response of cavity-embedded QW excitons, which is determined only by the degree of cooperation in the bright state. This is measured by an effective number of wells, which can be calculated by summing the squared electric field at the QW positions, and is given by [54,38,40]

$$N_{\text{eff}} = \frac{N}{2} \pm \frac{1}{2} \frac{\sin Nkl}{\sin kl}, \quad (25)$$

where the upper (lower) sign is appropriate for a symmetric (antisymmetric) electric field inside the microcavity, and l indicates the period of the multiple QW. By working to linear order in Γ_0 (which amounts to neglecting multiple interferences between the wells) all the previous formulas remain valid, provided Γ_0 is replaced with $N_{\text{eff}}\Gamma_0$. An exact formalism considering additional polariton modes arising due to the radiative coupling between different wells is developed in [40], and the case of two non-identical QWs in a microcavity including radiative coupling is studied in [35,61].

In principle all quantities appearing in the previous equations depend on angle and/or polarization: exciton frequency ω_{ex} , cavity–mode frequency ω_m^α , cavity mode linewidth γ_m , exciton–photon matrix element V . However in practice the angle and polarization dependence of ω_m is by far the dominant effect. In fact ω_{ex} may be taken as independent of angle, since spatial dispersion of the exciton is negligible at the small internal angles accessible to optical experiments. Also, V and γ_m can be seen to change only by a few percent even at large external angles; since both quantities are usually of the order of a few meV or smaller, their variation with angle is a small fraction of a meV and can be neglected.

4.3. Experiments. The experiments were carried out on a sample [62] consisting of a one-wavelength (λ) GaAs cavity sandwiched by 20 period $\lambda/4$ Al_{0.13}Ga_{0.87}As/AlAs DBRs. The top and bottom DBR were p- and n-doped, respectively. The cavity contains a set of centrally placed 10 nm wide In_{0.13}Ga_{0.87}As QWs with 10 nm barriers. The structure was grown by metal-organic vapour phase epitaxy (MOVPE) on a GaAs substrate. The sample was placed in a cryostat with angular access of $\sim 130^\circ$, permitting values up to $\theta = 60^\circ$ to be achieved. White light illumination from a projector lamp with angular spread $< 1^\circ$ was employed. The reflected light was dispersed by a grating spectrometer, and detected by a Ge photodiode.

The real structure differs from the one assumed in the theoretical treatment (Fig. 3, *a*) due to the presence of the GaAs substrate. Thus the cavity structure is slightly

unbalanced: the incident beam impinges on the top mirror (air side) with a calculated reflectivity $R_1 = 0.9964$, whereas the bottom mirror (substrate side) has a reflectivity $R_2 = 0.9874$ [63]. As already remarked, the main effect of unbalancing is that reflectivity dips are much less pronounced and do not reach zero; the previous expressions for mode energies in the high-reflectivity limit remain unchanged, however.

A series of polarization-resolved reflectivity spectra at different angles was shown in Fig. 1 of [41]. We just recall the main features: at low angles the cavity mode (C) is at lower energy compared to the exciton (X), which appears weakly in reflectivity. On increasing the angle the cavity mode shifts to higher energy and an anticrossing behavior typical of the strong-coupling regime is seen. The two reflectivity dips have equal intensities at an angle $\theta = 30^\circ$; at this angle mixed cavity polaritons with equal exciton and photon amplitudes are realized. For larger angles the cavity mode rapidly shifts to higher energy and the exciton is again barely visible.

With increasing angle the reflectivity dips become more pronounced for TM and less pronounced for TE polarization. This can be understood from Eqs. (A2) and (A5), since the reflectivity R_1 of the top mirror increases with angle for TE and decreases for TM polarization (while R_2 has a smaller variation with angle due to the presence of the substrate): thus the cavity becomes more unbalanced for TE and less unbalanced for TM, thereby explaining the trend of reflectivity dips [64]. This also implies that in an unpolarized experiment the TM component dominates in determining the position of reflectivity structures (see Sec. 5.3). An analysis of linewidths and their angular dependence and a numerical transfer matrix fit to the dip intensities are presented in [41].

In Fig. 4 we show the measured and calculated dispersion of cavity polaritons for both polarizations. The calculations were made using the analytic formulas of the previous Sections and of Appendix A, for a symmetric structure with $N = 20$ quarter-wave pairs in each DBR. The cavity and DBR layer thicknesses were slightly adjusted in order to account for the observed mode energies and polarization splitting: we used $L_c = 257$ nm, $a = 73$ nm, $b = 63.8$ nm. These values are consistent with wide-band reflectivity spectra, as discussed below. The energy-dependent refractive indices are taken from the 300 K data of [65], decreased by 1.3% for use at 10 K. At 8650 Å the values are 3.5467 for GaAs and 3.0108 for AlAs; the refractive index of GaAs increases by about 0.9% from 1.40 to 1.45 eV [65]. For the QW exciton $\omega_{\text{ex}} = 1415.4$ meV, $f_{xy} = 4.2 \cdot 10^{12}$ cm⁻² [66], leading to $\Gamma_0 = 0.052$ meV, with three QWs and $N_{\text{eff}} = 2.52$. We also take $\gamma_{\text{ex}} = 0.9$ meV from the experimental linewidth of the exciton (FWHM ~ 1.8 meV).

The first feature to be noticed is the anticrossing at $\theta \simeq 30^\circ$, with a Rabi splitting of ~ 5 meV. The penetration depth is calculated to be $L_{\text{DBR}} = 780$ nm and the effective length $L_{\text{eff}} \simeq 1.04$ μm, yielding a Rabi splitting

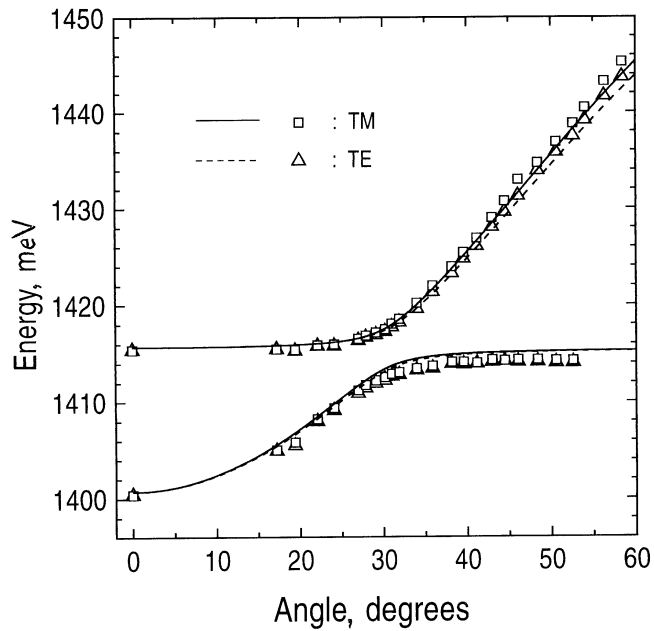


Рис. 4. Dispersion of cavity polaritons in a GaAs cavity with three $\text{In}_{0.13}\text{Ga}_{0.87}\text{As}$ QWs and $\text{AlAs}/\text{Al}_{0.13}\text{Ga}_{0.87}\text{As}$ mirrors. Continuous and dashed lines are the theoretical curves for TM and TE polarizations respectively; squares and triangles are the experimental data from positions of reflectivity dips.

$2\hbar V = 4.7$ meV, in good agreement with the experimental value. The Rabi splitting for QW excitons in microcavities yields an accurate measurement of the oscillator strength through formulas (21)–(22), provided the penetration depth in the dielectric mirrors is properly taken into account.

Next we consider the polariton dispersion at high angles (where it almost coincides with the cavity-mode dispersion). The energy dependence of the index of refraction, although weak, is crucial for obtaining good agreement with the experimental results. This can be understood from Eq. (15) (neglecting the TM–TE difference for the moment). If the refractive index is taken to be independent of energy, the effective index is $n_{\text{eff}} \simeq 3.25$ and the cavity-mode frequency at $\theta = 60^\circ$ would be 1454 meV, which is about 10 meV higher than the experimental result. A similar discrepancy was noticed before [54] and could not be explained. However since the effective index increases by 0.7% from 1.4 to 1.45 eV, the use of formula (15) leads to a cavity-mode energy of 1444 meV at $\theta = 60^\circ$, in agreement with the experimental value. Thus including the energy-dependence of the index of refraction fully solves the problem of mode dispersion at high angles. We also note that the strong sensitivity of the cavity-mode energy to the refractive index in the DBR layers through $\omega_s(0)$ implies that a weak nonlinearity in one of the DBR layers might be amplified and give rise to a strong nonlinear response of the microcavity system [67].

Finally we turn to the polarization splitting. Experimentally the TM mode is higher in energy; the

TM–TE splitting of the upper cavity polariton is ~ 1.7 meV at the largest angle $\theta = 60^\circ$. From the discussion of Sec. 4.1, and in particular Eq. (16), this implies that the frequency of the center of the stop band ω_s is greater than the bare Fabry-Pérot frequency ω_c . This expectation is confirmed by wide-band reflectivity spectra where the cavity dips are found to be displaced to lower energy relative to the center of the stop band by ~ 10 meV, implying $\omega_c < \omega_s$. Furthermore the parameters we employ for our calculations give $\omega_c = 1.358$ eV and $\omega_s = 1.409$ eV at $\theta = 0$, consistent with both the experimental deduction of $\omega_c < \omega_s$ from the wide band spectra, and with the observed sign of the TM–TE splitting. The angular dependence of the splitting is then controlled by the penetration depths (see inset of Fig. 2). Using the same set of parameters as before, in Fig. 5 we compare the calculated TM–TE splitting of upper and lower cavity polaritons with the experimental results. The formation of mixed exciton-cavity modes around $\theta = 30^\circ$ is also reflected in the TM–TE splitting, which has a peculiar behavior in the anticrossing region. The polarization splitting of the bare cavity mode increases like $\sin^2 \theta_{\text{eff}}$ (see Eq. (17)): this behavior appears outside the anticrossing region for the lower polariton at low angles, and for the upper polariton at large angles. Although the experimental results show some unavoidable spread (note the scale on the energy axis), agreement between experiment and theory is very satisfactory. Thus the comparison of calculated and measured polarization splitting confirms the accuracy of the analytic treatment.

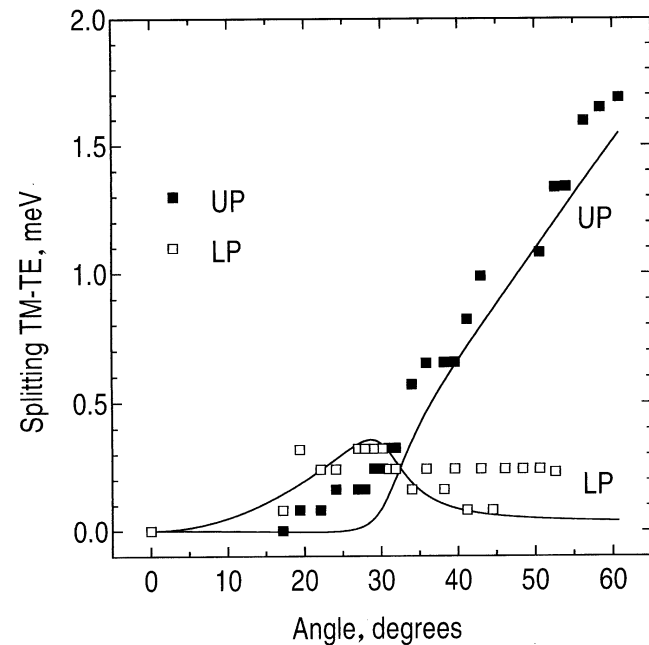


Рис. 5. TM–TE polarization splitting of upper and lower polaritons in the GaAs cavity of Fig. 4, with the same parameters. Continuous lines: theoretical curves; closed and open squares: experimental data.

5. Coupled microcavities

5.1. Empty, coupled cavities. We will now derive formulas for the energies and widths of the cavity–modes for two empty coupled microcavities. We first consider a symmetric structure (see Fig. 3, *b*): this requires that the left and right DBRs are the mirror image of each other, and that the two cavities have the same length L_c , so that both photon eigenmodes have the same frequency ω_m and width (HWHM) γ_m in the absence of coupling. The number of quarter-wave pairs in the symmetric central mirror is half-integer: we denote it by $N_c - 1/2$ (cfr. Fig. 3, *b*).

The central mirror couples the two degenerate modes at ω_m of the isolated cavities and breaks their degeneracy. Due to the symmetry of the system, the cavity modes may be classified as symmetric (*S*) and antisymmetric (*A*). Their complex energies are given in the limit $R, R_c \rightarrow 1$ by (see Appendix B for a derivation)

$$\omega = \omega_j - i\tilde{\gamma}_m = \omega_m + (-1)^j V_{\text{opt}} - i\tilde{\gamma}_m, \quad j = 1, 2, \quad (26)$$

with

$$V_{\text{opt}} = \frac{c\sqrt{1-R_c}}{2n_c L_{\text{eff}} \cos \theta_c} \quad (27)$$

representing the coupling constant between the two cavities, and

$$\tilde{\gamma}_m = \frac{c(1-R)}{4n_c L_{\text{eff}} \cos \theta_c}. \quad (28)$$

R and R_c are the reflectivities of the external and central mirrors, respectively, dependent on both angle and polarization. For even N_c the symmetric mode lies at higher energy than the antisymmetric one, while for odd N_c the reverse is true (we are now specifying to the case $n_1 < n_2$, otherwise the identification of *S* and *A* mode is interchanged). Equation (26) follows from diagonalizing a 2×2 Hamiltonian, which describes two identical cavity modes coupled by a matrix element V_{opt} . The angular dependence of R_c for the two polarizations (see Appendix A) is such that V_{opt} increases with angle for TM, and decreases for TE polarization.

Comparison with the single cavity case shows that the mode widths in the coupled cavity structure are *reduced* by a factor of two: the physical interpretation of this result (which is rigorously derived in Appendix B) is that the decay rate of the coupled cavity mode is the average of that of left and right cavities, but each cavity mode can now decay on one side only of the coupled structure. The predicted reduction in coupled-cavity linewidth is however difficult to observe, since it requires comparing the optical behavior of two different samples.

When the two cavities have different lengths, it is no longer possible to speak of a symmetric and an antisymmetric mode: the thicker (thinner) cavity has a larger weight in the low (high) energy mode. We show here that the combined effects of cavity mismatch and absorption give rise to differing intensities of the reflectivity dips. The dip intensities can be calculated analytically [68] also when

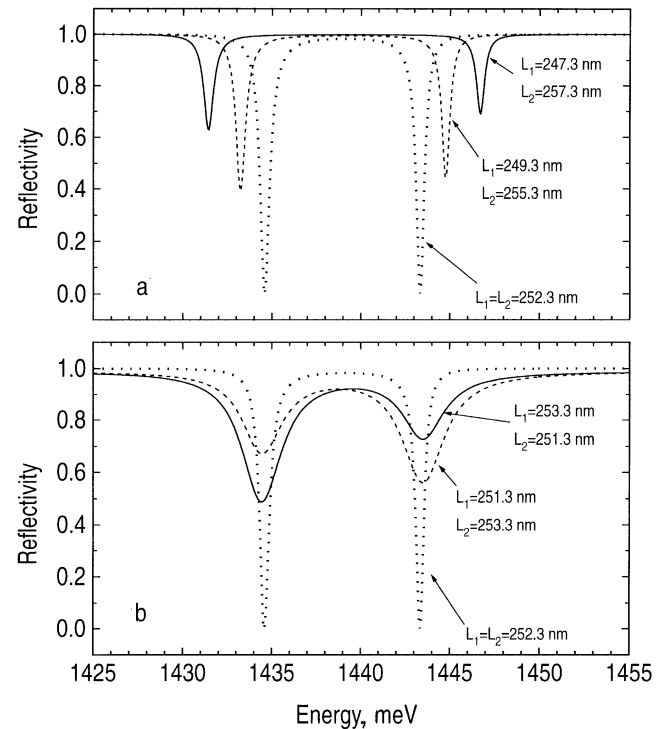


Рис. 6. Calculated normal incidence reflectivity for two empty coupled GaAs microcavities. (*a*) Each layer in the structure is described by a real refractive index. (*b*) The GaAs layers are described by a complex refractive index with an imaginary part $\kappa = 0.005$.

the refractive index is assumed to have an imaginary part, and the results are as follows. Since in the presence of absorption it is the top (outer) cavity which gives the largest contribution to the reflectivity spectrum, the corresponding peak is stronger. On the other hand the relative intensities in the transmission spectrum do not depend on which cavity is thicker. These conclusions confirm the results obtained by numerical simulations in [31].

This behaviour is illustrated in Fig. 6, which displays the normal incidence reflectivity of two coupled GaAs microcavities with AlAs/GaAs mirrors. Fig. 6, *a* is calculated for a real refractive index, while Fig. 6, *b* includes absorption through an imaginary part $\kappa = 0.005$ of the refractive index in the GaAs layers. Fig. 6, *a* demonstrates that the cavity mismatch alone yields reflectivity dips which are much less pronounced, since the structure is now unbalanced, but produces only a small asymmetry (unless the cavity mismatch is very large). Furthermore the reflectivity spectra are the same from both sides, irrespective of which cavity is thicker (this is implied by the general form (3) of the transfer matrix for a non-absorbing structure). In Fig. 6, *b* the cavity mismatch is taken to be much smaller than in Fig. 6, *a* (thus the dip positions are almost unchanged), but nevertheless the two dips are much broader and have different intensities: thus even a small cavity unbalancing does produce a sizeable peak broadening and asymmetry when combined with a finite imaginary part

of the refractive index. Moreover, the reflectivity spectra change when the order of the cavities is changed: when the top cavity is thinner (dashed line) the dip at higher energy is stronger than the dip at lower energy, while when the top cavity is thicker (solid line) the lower dip is stronger. These conclusions will be important for interpreting the experimental results of Sec. 5.3.

5.2. Coupled cavities with quantum wells. We now consider two identical microcavities of length $L_c = \lambda$, each containing a QW at the antinode of the electric field (see Fig. 3, *b*). Because of the symmetry of the system, the dispersion equations for exciton-polaritons in two coupled microcavities can be written again as two independent equations for symmetric and antisymmetric polariton modes:

$$\frac{\Gamma}{\Delta} = \frac{-i(\sqrt{RR_c} - \sqrt{R_c}e^{-i\chi} + \sqrt{R}e^{i\chi} - e^{-2i\chi}) \pm \sqrt{1 - R_c}(e^{-i\chi} + \sqrt{R})}{(1 + \sqrt{R}e^{i\chi})(1 + e^{-2i\chi} + 2\sqrt{R_c}e^{-i\chi})}, \quad (29)$$

with $\chi = \frac{n_c}{c}L_{\text{eff}}(\omega - \omega_m) \cos \theta_c$. Expanding the r.h.s in (29) up to first order in $(\omega - \omega_m)$, we find that the two equations reduce to

$$(\omega - \omega_{\text{ex}} + i\gamma_{\text{ex}})(\omega - \omega_m + V_{\text{opt}} + i\tilde{\gamma}_m) = V^2, \quad (30)$$

$$(\omega - \omega_{\text{ex}} + i\gamma_{\text{ex}})(\omega - \omega_m - V_{\text{opt}} + i\tilde{\gamma}_m) = V^2, \quad (31)$$

with the coupling V_{opt} between the two cavities and the linewidth $\tilde{\gamma}_m$ given by (27) and (28), respectively. The effective coupling V represents the exciton-cavity mode interaction and is calculated to be

$$V^2 = \frac{2\Gamma_c}{n_c L_{\text{eff}} \cos \theta_c} \frac{(1 + \sqrt{R})^2(1 + \sqrt{R_c})}{(R + 1 + 4\sqrt{R} + 2\sqrt{RR_c})}. \quad (32)$$

In the limit $R, R_c \rightarrow 1$, V reduces to (21) for TE or to (22) for TM polarization, i.e. it coincides with the coupling constant for the single QW embedded in a microcavity.

It is interesting and useful to interpret the results in terms of an oscillator model. The twofold-degenerate lowest exciton state in two identical and uncoupled QWs has the symmetric and antisymmetric eigenfunctions

$$|S\rangle = (|QW1\rangle + |QW2\rangle)/\sqrt{2}, \quad (33)$$

$$|A\rangle = (|QW1\rangle - |QW2\rangle)/\sqrt{2}, \quad (34)$$

where $|QW1\rangle$ and $|QW2\rangle$ are the single exciton wave functions in the two QWs. On the other hand, as already stated, coupling between the two photon modes at equal frequency ω_m leads to the formation of symmetric and antisymmetric coupled cavity modes, with complex frequencies given by Eq. (26). The symmetric exciton state only interacts with the symmetric photon mode, and the antisymmetric exciton only interacts with the antisymmetric photon mode: since the coupled cavity frequencies do not coincide, there are four distinct exciton-polariton states which may be observed in reflection.

The two coupled cavities with QWs are therefore described by a four-oscillator model, whose hamiltonian can be written as

$$\begin{bmatrix} \omega_m - i\tilde{\gamma}_m & V_{\text{opt}} & V & 0 \\ V_{\text{opt}} & \omega_m - i\tilde{\gamma}_m & 0 & V \\ V & 0 & \omega_{\text{ex}} - i\gamma_{\text{ex}} & 0 \\ 0 & V & 0 & \omega_{\text{ex}} - i\gamma_{\text{ex}} \end{bmatrix} \quad (35)$$

in the basis of localized cavity and exciton states. Equation (35) includes all the couplings between the four oscillators present in the system. It also allows for generalizations, like having different cavity parameters (in which case ω_m differs for the two cavities) or different QW excitons (in this latter case ω_{ex} would have two different values). By changing basis to the states (33)–(34) for the exciton and the analogous ones for the cavity states, the hamiltonian (35) takes a 2×2 block form in which symmetric or antisymmetric exciton states of energy $\omega_{\text{ex}} - i\gamma_{\text{ex}}$ are coupled by a matrix element V to symmetric or antisymmetric cavity modes of energy $\omega_m \pm V_{\text{opt}} - i\tilde{\gamma}_m$, leading again to Eqs. (30)–(31). The simple physical model used in the first of [33] is therefore recovered.

5.3. Experiments. The coupled cavity structure was grown by MOVPE and consists of two λ -thick GaAs cavities (nominal thickness $L_c = 250$ nm) and three GaAs/AlAs dielectric mirrors. The top DBR contains 12 periods, the central one 14.5 (thus $N_c = 15$) and the bottom DBR 17.5 periods, ending on a GaAs substrate. Each cavity contains three 10 nm wide $\text{In}_{0.06}\text{Ga}_{0.94}\text{As}$ QWs separated by 10 nm GaAs barriers. The number of periods in the central mirror was chosen in order to achieve an optical splitting between symmetric and antisymmetric cavity modes of the order of the Rabi splitting: this maximizes the effect of coupling between the four oscillators present in the system, and allows the removal of degeneracy of exciton states to be achieved, as is shown below. The different number of periods in the top and bottom DBRs partially compensates for the presence of the substrate. The main effect of asymmetry in the real structure is again in determining the absolute values of reflectivity dips, which is not the main issue here. We also remark that in these high-finesse microcavities absorption is rather strong so that transmission, although measurable, is usually only a few per cent; therefore in order to make a detailed and reliable comparison between experiment and theory we chose to concentrate on reflectivity results.

In Fig. 7, *a* we show the measured unpolarized reflectivity spectra at different angles. At the lowest angle $\theta = 10^\circ$ the symmetric and antisymmetric cavity modes are clearly seen, together with a weak exciton feature. The unsplit exciton peak indicates that the two sets of QWs have nearly the same exciton energies; on the other hand the different intensities of the two cavity peaks point to slightly different values for the cavity lengths, with the top cavity being thicker. On increasing the angle the two cavity modes shift to higher energies and gradually mix with the exciton states.

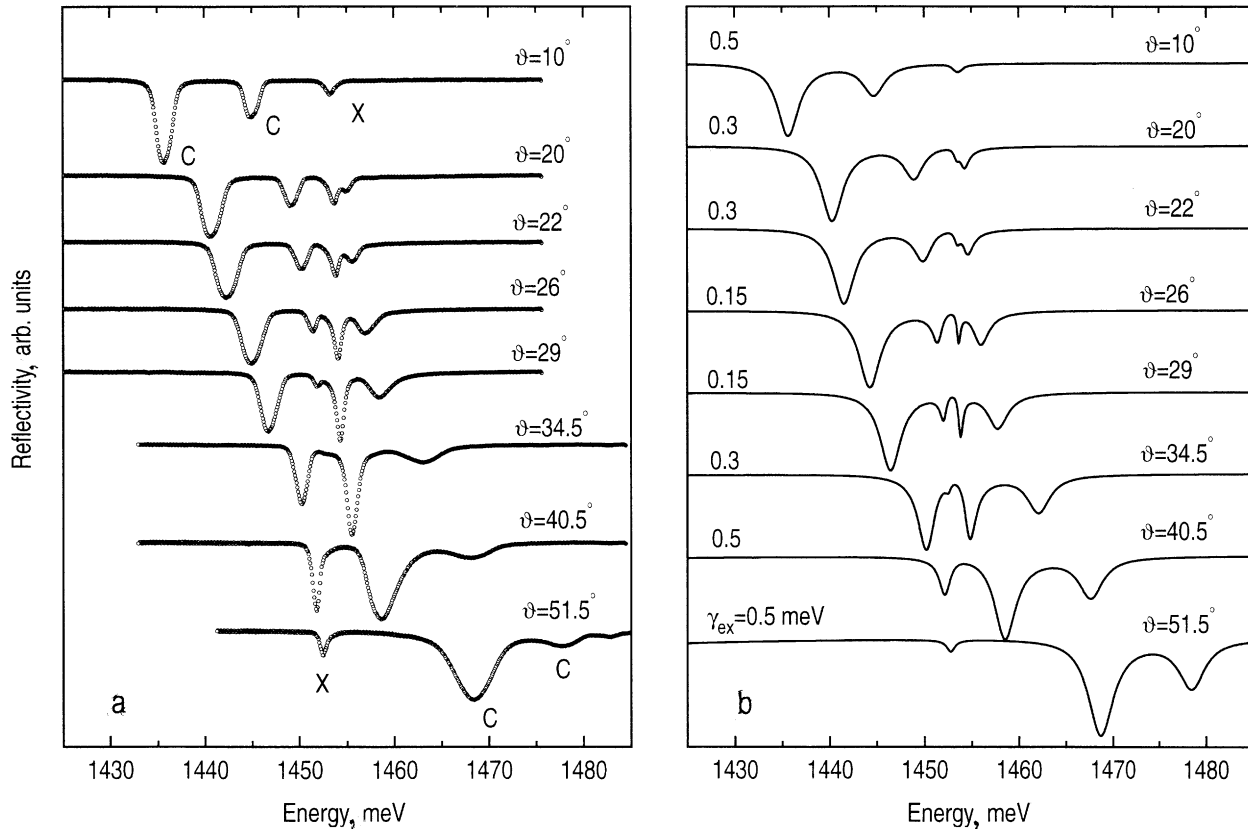


Рис. 7. Measured (a) and calculated (b) reflectivity spectra as a function of angle for two coupled GaAs cavities each containing three $\text{In}_{0.06}\text{Ga}_{0.94}\text{As}$ QWs. Parameters are given in the text and above the curves.

At $\theta = 20^\circ$ the exciton states appear as two peaks split by about 2 meV: the removal of degeneracy of spatially separated exciton states has been achieved. For angles around $\theta = 30^\circ$ the four states are strongly mixed and can no longer be attributed to distinct exciton and cavity states. It is interesting to observe that the third peak becomes narrower in the resonance region: this feature will be discussed in more detail below. For $\theta > 40^\circ$ the cavity modes are at higher energies than the excitonic states, which again become degenerate. The relative intensity of the cavity modes is similar to that at low angles; however the dips are broader, since the cavity modes are now degenerate with the excitonic continuum in the QWs [7].

We notice that the two energetically split excitonic states are both observed in reflectivity spectra, i.e., they are both "bright". This is a new situation compared to the single cavity case, where if the QW excitons are identical only one state is bright and the remaining ones are dark and unobservable (see discussion of Sec. 4.2). Thus the double cavity configuration allows a qualitatively new phenomenon to be obtained, namely a sizeable radiative splitting between bright excitonic states, which cannot be observed either for free QWs nor for QWs in a single cavity.

Fig. 7, b shows the calculated reflectivity curves at the same angles for TM polarization (which dominates the unpolarized spectra, as for the single cavity case).

Parameters are chosen as follows: cavity lengths $L_1 = 253.6$ nm, $L_2 = 251$ nm, DBR layers $a = 70.34$ nm, $b = 59.52$ nm (close to nominal values, and again adjusted to reproduce mode energies and polarization splittings). The penetration depth and effective length at $\theta = 0$ are $L_{\text{DBR}} = 670$ nm and $L_{\text{eff}} = 922$ nm. The reflectivity of the central mirror is $R_c = 0.97$ (note that Eqs. (A2), (A5) apply also to a symmetric mirror, taking $N = N_c$, provided the number of quarter-wave pairs is $N_c - 1/2$ as in Fig. 3, b), leading to an optical matrix element $V_{\text{opt}} = 5.2$ meV. An imaginary part $\kappa = 0.005$ has been added to the index of refraction for the GaAs layers.

The choice of the excitonic parameters is important. The exciton frequency is $\omega_{\text{ex}} = 1453$ meV. The exciton halfwidth is taken to be different for each curve, in order to account for the effect of resonance narrowing; starting from the experimental value $\gamma_{\text{ex}} = 0.5$ meV (HWHM) at low and high angles, reproducing the width of the third peak requires values of γ_{ex} down to 0.3 or 0.15 meV at resonance (the values of γ_{ex} are indicated on each curve). The oscillator strength per unit area is $f_{xy} = 4.2 \cdot 10^{12} \text{ cm}^{-2}$ leading again to a radiative width $\Gamma_0 = 0.052$ meV for the sets of three QWs. Note that the oscillator strength of excitons in $\text{In}_x\text{Ga}_{1-x}\text{As}/\text{GaAs}$ QWs of ~ 10 nm width is almost independent of In concentration [66]. The exciton-cavity matrix element for each QW is calculated to be

$V = 2.5$ meV. We also account for absorption in the excitonic continuum by adding a further contribution to the imaginary part of the refractive index in the QW regions, for energies $E_b \sim 8$ meV above the excitonic transition energy [66]. From the known absorption probability for interband transitions, which is $w \simeq 0.7\%$ for the heavy-hole to conduction band transition [69,70], we obtain an absorption coefficient $\alpha = 7 \cdot 10^3 \text{ cm}^{-1}$ and a value $\kappa = 0.05$.

The calculated reflectivity curves reproduce the important features of the experimental spectra of Fig. 7, *a*. The relative intensities of the cavity modes at low or high angles is explained by the combination of cavity mismatch and absorption in the GaAs layers, following the theoretical discussion of Sec. 5.1: the most pronounced dip is the lowest energy one, corresponding to the top cavity being thicker. The observed increase of linewidth of the cavity dips at high angle is reproduced by the calculation when absorption of the excitonic continuum is included. Furthermore, in the resonance region the anticrossing behavior and the change of relative intensities of the various peaks is reproduced very well; the linewidth of the third peak agrees with the observed one, but only when a very narrow excitonic homogeneous broadening is assumed. Thus the present results give further evidence for the occurrence of line narrowing of cavity polaritons at resonance. This was first attributed to "motional" narrowing due to the very light in-plane mass of cavity polaritons [16,17]; recently it has been shown [18–21] that a resonance narrowing occurs also for any mechanism of inhomogeneous broadening of the exciton line, although the "motional" effect is necessary to eliminate scattering between low- k polariton states.

It can be noticed from Fig. 7 that the relative intensities of the various dips are well reproduced by the calculation, but the intensity of the third dip is not large enough when compared to that of the fourth dip. In order to examine this question and the resonance narrowing in more detail, in Fig. 8 we show an enlarged view of the reflectivity in the resonance region for $\theta = 26^\circ$. The experimental result is compared to three different calculations. In the first one (curve (a)) the off-resonance excitonic linewidth $\gamma_{\text{ex}} = 0.5$ meV is taken: this is seen to be inadequate as the third peak is too weak and its linewidth is too large. In the second calculation (curve (b)) the narrower halfwidth $\gamma_{\text{ex}} = 0.15$ meV is assumed: now the width of the third peak is close to the experimental one, and its intensity is increased, but still being a bit weaker than in the experiment. As a possible explanation for the intensity of the third peak we introduce a small energy difference of 1 meV of the two QW excitons (curve (c)), with the QW of the inner cavity being at higher energy. In this case the third peak moves closer in energy to the fourth one and gains part of its oscillator strength, thereby leading to an intensity ratio which is very similar to the experimental one. We should also say that other explanations cannot be ruled out; reproducing the observed intensities at resonance in all details would probably require a more realistic model

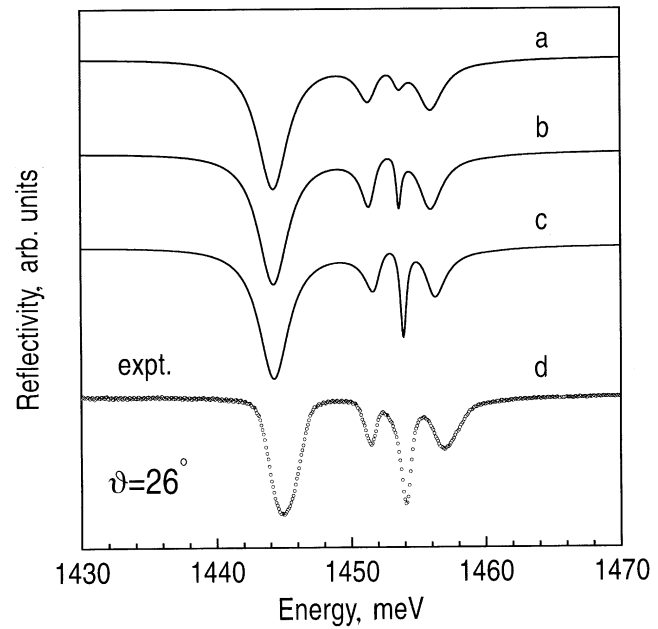


Рис. 8. Reflectivity lineshape in the resonance region at an angle $\theta = 26^\circ$ for the two coupled GaAs cavities. Curve (a): theory, $\gamma_{\text{ex}} = 0.5$ meV, identical QWs ($\hbar\omega_{\text{ex}} = 1453$ meV). Curve (b): theory, $\gamma_{\text{ex}} = 0.15$ meV, identical QWs. Curve (c): theory, $\gamma_{\text{ex}} = 0.15$ meV, $\hbar\omega_{\text{ex}} = 1453$ meV for the QWs of the top cavity, $\hbar\omega_{\text{ex}} = 1454$ meV for the QWs of the bottom cavity. Curve (d): experimental results.

of excitonic broadening, including e.g. an inhomogeneous distribution of excitonic levels [18,29,71] which goes beyond our simple Lorentzian model.

In Fig. 9 the cavity polariton dispersion measured from the position of unpolarized reflectivity dips is compared to the one calculated for both TE and TM polarizations. Here in order to use the analytic formulas we have assumed the symmetric structure shown in Fig. 3, *b*, with a thickness $L_c = 252.3$ nm and $N = 12$ pairs in the external DBRs. Several features can be seen. At $\theta = 10^\circ$ the symmetric and antisymmetric coupled-cavity modes are well separated from the exciton resonance and have an energy of 1435.5 and 1445 meV, respectively, close to the values at normal incidence; the optical splitting of cavity modes is thus $2V_{\text{opt}} = 9.3$ meV. The same value for the optical splitting is also obtained at an angle $\theta = 50^\circ$, when the two cavity modes are outside the anticrossing region and at much higher energy than the exciton. At intermediate angles strong interaction between the four oscillators occurs. The antisymmetric cavity mode interacts with the antisymmetric linear combination of exciton states and anticrossing occurs at $\theta \simeq 22^\circ$, with a Rabi splitting of ~ 5 meV: this is reproduced well by the calculation using the known exciton oscillator strength, as in the single cavity case. Anticrossing between the symmetric cavity- and exciton modes occurs at $\theta = 35^\circ$ with the same Rabi splitting ~ 5 meV. The two anticrossings are indicated by arrows on the plot. Thus both the optical matrix element V_{opt} and the exciton-

cavity matrix element V can be read directly from the dispersion curves and are close to the calculated values. The experimental dispersion at high angles agrees well with the calculated one and is closer to that for TM polarization, as discussed in Sec. 4 and in [64]. This corresponds to the previous considerations, that the position of reflectivity dips in unpolarized spectra is mostly determined by TM polarization. Finally, we remark that good agreement at high angles depends critically on inclusion of the energy dependence of the index of refraction, as in the single-cavity case: when this is neglected, the calculated dispersion turns out to be much steeper than the experimental one.

In Fig. 10 we present an example of polarization-resolved reflectivity spectra at the largest measured external angle $\theta = 51.5^\circ$. The exciton peak is seen to be unsplit, since the interaction between exciton and cavity modes is weak. The peaks labelled "C" represent optically coupled modes of the two cavities. We first remark that the lower energy cavity dips are much more intense for both polarizations: this is due to a slightly larger thickness of the top cavity combined with the presence of absorption, as already discussed. Both the lower (symmetric) and upper (antisymmetric) coupled cavity modes have a polarization splitting, the TM mode being higher in energy than the TE one; the splitting is larger for the upper cavity peak. These features, as well as the relative intensities, are reproduced well by the calculation. The energy positions of the structures depend on polarization through the isolated cavity mode $\omega_m^\alpha(\theta)$ as well as the optical coupling V_{opt}^α (Eq. (27)); the inset in Fig. 10 illustrates the evolution of the polarization splitting

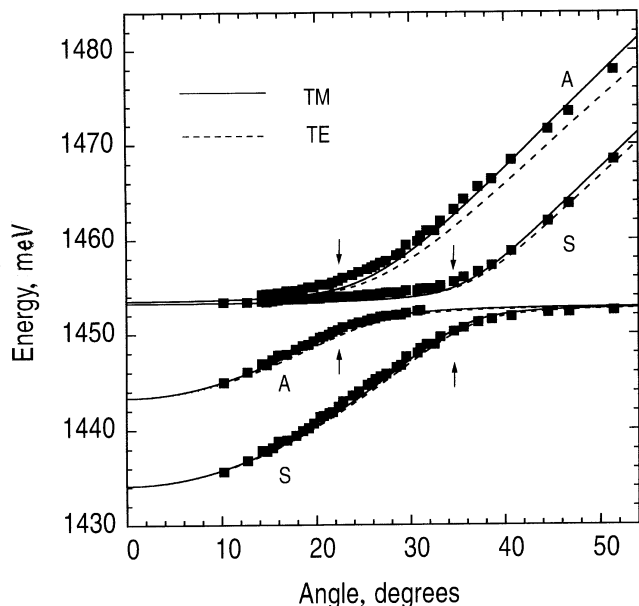


Fig. 9. Dispersion of cavity polaritons for the two coupled GaAs cavities of Figs. 7 and 8 each containing three InGaAs QWs. Parameters are given in the text. Continuous and dashed lines: theoretical curves (solid = TM, dashed = TE); squares: experimental data. The arrows denote the separate anticrossings of A and S modes.

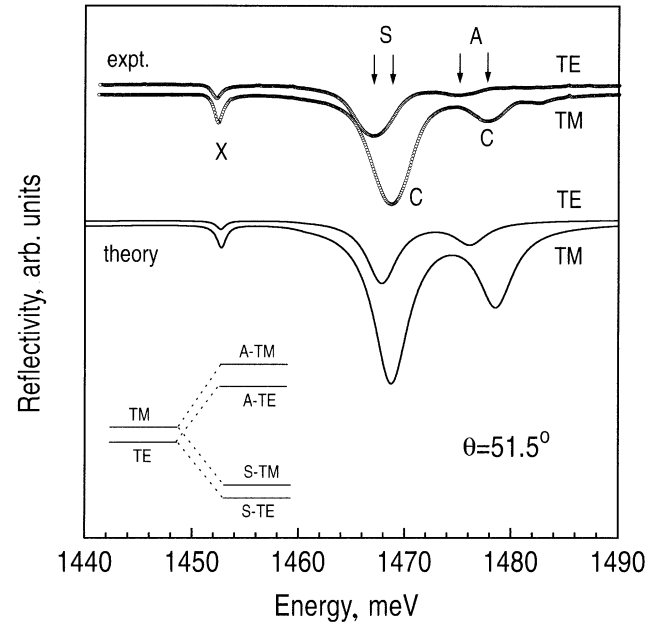


Fig. 10. Experimental and theoretical reflectivity curves for the GaAs coupled cavities at $\theta = 51.5^\circ$, for TE and TM polarizations. Inset: schematic illustration of polarization splitting of the optical modes in a single cavity (left) and in coupled cavities.

from the single to the coupled cavity for the present case of odd N_c . The polarization splittings of the upper and lower doublet are calculated as

$$\Delta\omega_A = \Delta\omega_m + V_{\text{opt}}^{\text{TM}} - V_{\text{opt}}^{\text{TE}} = 2.2 \text{ meV}, \quad (36)$$

$$\Delta\omega_S = \Delta\omega_m - V_{\text{opt}}^{\text{TM}} + V_{\text{opt}}^{\text{TE}} = 0.8 \text{ meV}, \quad (37)$$

respectively. The predicted order of levels is the same as in the experimental result, namely S-TE, S-TM, A-TE, A-TM on increasing energy. Note that this is not a general property, since it depends on the polarization splitting for the single cavity (which can have either sign) as well as on the size of V_{opt}^α . The splitting of the antisymmetric mode is larger because the optical matrix element V_{opt} is larger for TM polarization (see also the inset). The experimental values of the polarization splittings are $\Delta\omega_A = 2.5 \text{ meV}$ for the upper doublet and $\Delta\omega_S = 1.7 \text{ meV}$ for the lower doublet, in fair agreement with the values given in (36)–(37). Thus we can conclude that a good understanding of polarization splitting of coupled cavities has been achieved.

6. Conclusions

Angle- and polarization-resolved spectroscopy on microcavities with QWs yields very detailed information about exciton-light coupling in the strong-coupling regime. Interpreting cavity-polariton spectroscopy at meV or sub-meV level requires the inclusion of several effects: reflection phase delay in the dielectric mirrors, angle- and polarization dependence of mode frequency and of exciton-cavity coupling, energy dependence of the refractive

index, and optical coupling between the cavities, which are analyzed in the present paper mainly on the basis of analytic results. The theoretical formulation based on semiclassical theory can be easily extended or applied to other related situations.

The energy of single-cavity modes is determined by the bare Fabry-Pérot frequency ω_c and by the center of the stop band ω_s , weighted with their characteristic lengths: the penetration depth in the dielectric mirrors carries a nontrivial angle- and polarization dependence. The polarization splitting of single-cavity mode depends on the mismatch between ω_c and ω_s , and increases with internal angle like $\sin^2 \theta_{\text{eff}}$. When QWs are embedded in the microcavity at an antinode of the electric field, the exciton and cavity mode are described at each angle by a two-oscillator model, whose parameters are expressed in terms of microscopic properties of the exciton and structural parameters. Weak and strong coupling regimes and the formation of cavity polaritons are described. Comparison with experimental results on a GaAs-based cavity with $\text{In}_{0.13}\text{Ga}_{0.87}\text{As}$ QWs shows that a good understanding of the exciton-cavity mode interaction, polariton dispersion and polarization properties has been achieved. For the polariton dispersion it is important to include the energy dependence of the index of refraction, which makes the cavity mode considerably less steep at high angles.

Coupling of two identical cavities through a central mirror induces an optical splitting between symmetric and antisymmetric modes, which also depends on angle and polarization. A mismatch of cavity lengths combined with absorption in the structure leads to different intensities of reflectivity dips. When QW excitons are embedded in both cavities at antinode positions, the system behaves as four coupled oscillators, leading to a removal of degeneracy of exciton states separated by a macroscopic distance. The energetically split excitonic oscillators are both bright and observable, unlike the situation for two identical QWs in free space or in a single cavity. If the two cavities (and the two QWs) are identical, separate anticrossing of symmetric and antisymmetric modes occurs. These features are confirmed by experimental results on a coupled GaAs cavity with $\text{In}_{0.06}\text{Ga}_{0.94}\text{As}$ QWs. The polariton dispersion for coupled cavities is well described by theory; a lineshape analysis allows an effect of line narrowing of cavity polariton linewidths in the resonance region to be revealed. Finally, the polarization splitting of coupled-cavity system has been analyzed in detail and is shown to depend both on single-cavity factors and on angle- and polarization dependence of the optical coupling. Inclusion of all these effects provides a good description of the experimental results.

Acknowledgements

The authors are indebted to D.M. Whittaker for many helpful discussions and for pointing out the importance of inclusion of the energy dependence of the refractive indices to fit the cavity-mode dispersion. The work at Sheffield was supported by EPSRC grant GL/L32187.

Appendix A: Parametrization of DBR reflection coefficient

Evaluation of the quantities appearing in the parametrization of the DBR reflectivity, Eq. (10), requires expanding the elements of the transfer matrix up to linear order in terms of two small parameters ε_1 and ε_2 defined as follows:

$$\begin{aligned}\varepsilon_1 &= \frac{n_1}{c} a(\omega \cos \theta_1 - \omega_{1s}), \\ \varepsilon_2 &= \frac{n_2}{c} b(\omega \cos \theta_2 - \omega_{2s}),\end{aligned}\quad (\text{A1})$$

where a, b are the thicknesses of DBR layers (see Fig. 1), and θ_1 and θ_2 are the angles in the layers with refractive indexes n_1 and n_2 respectively. The frequencies ω_{1s} and ω_{2s} are defined by $n_1\omega_{1s}a/c = n_2\omega_{2s}b/c = \pi/2$. Note that, as far as ω_{1s} may differ from ω_{2s} , our expressions can be used also when the $\lambda/4$ condition is not exactly satisfied. For the case $n_1 < n_2$, lengthy but straightforward calculations lead — for a large number N of periods — to the following expressions:

TE polarization:

$$R(\theta) = 1 - 4 \frac{n_{\text{ext}}}{n_c} \frac{\cos \theta}{\cos \theta_c} \left(\frac{n_1 \cos \theta_1}{n_2 \cos \theta_2} \right)^{2N}, \quad (\text{A2})$$

$$\omega_s(\theta) = \frac{\pi c}{2(a+b)} \frac{n_1 \cos \theta_1 + n_2 \cos \theta_2}{n_1 n_2 \cos \theta_1 \cos \theta_2}, \quad (\text{A3})$$

$$L_{\text{DBR}}(\theta) = \frac{2n_1^2 n_2^2 (a+b)}{n_c^2 (n_2^2 - n_1^2)} \frac{\cos^2 \theta_1 \cos^2 \theta_2}{\cos^2 \theta_c}. \quad (\text{A4})$$

TM polarization:

$$R(\theta) = 1 - 4 \frac{n_{\text{ext}}}{n_c} \frac{\cos \theta_c}{\cos \theta} \left(\frac{n_1 \cos \theta_2}{n_2 \cos \theta_1} \right)^{2N}, \quad (\text{A5})$$

$$\omega_s(\theta) = \frac{\pi c}{2} \frac{n_1 \cos \theta_2 + n_2 \cos \theta_1}{n_1 n_2 (a \cos^2 \theta_1 + b \cos^2 \theta_2)}, \quad (\text{A6})$$

$$L_{\text{DBR}}(\theta) = \frac{2n_1^2 n_2^2}{n_c^2} \frac{a \cos^2 \theta_1 + b \cos^2 \theta_2}{n_2^2 \cos^2 \theta_1 - n_1^2 \cos^2 \theta_2}. \quad (\text{A7})$$

At normal incidence, and if the $\lambda/4$ condition is exactly satisfied, we have

$$a = \frac{1}{4} \frac{\lambda_s}{n_1} \quad b = \frac{1}{4} \frac{\lambda_s}{n_2}, \quad (\text{A8})$$

where λ_s is the operating wavelength *in vacuum*; then the above formulas reduce to

$$R(0) = 1 - 4 \frac{n_{\text{ext}}}{n_c} \left(\frac{n_1}{n_2} \right)^{2N}, \quad (\text{A9})$$

$$\omega_s(0) = \frac{\pi c}{2(a+b)} \frac{n_1 + n_2}{n_1 n_2} = \frac{2\pi c}{\lambda_s}, \quad (\text{A10})$$

$$L_{\text{DBR}}(0) = \frac{2n_1^2 n_2^2 (a+b)}{n_c^2 (n_2^2 - n_1^2)} = \frac{\lambda_s}{2} \frac{n_1 n_2}{n_c^2 (n_2 - n_1)}, \quad (\text{A11})$$

and coincide with those given in [37,38].

The reflection coefficient for $n_1 > n_2$ may be similarly evaluated. In this case it is parametrized according to the lower sign in Eq. (10) of the text, and we obtain: TE polarization:

$$R(\theta) = 1 - 4 \frac{n_c \cos \theta_c}{n_{ext} \cos \theta} \left(\frac{n_2 \cos \theta_2}{n_1 \cos \theta_1} \right)^{2N}, \quad (\text{A12})$$

$$\omega_s(\theta) = \frac{\pi c}{2} \frac{n_1 \cos \theta_1 + n_2 \cos \theta_2}{n_1^2 a \cos^2 \theta_1 + n_2^2 b \cos^2 \theta_2}, \quad (\text{A13})$$

$$L_{\text{DBR}}(\theta) = \frac{2}{n_1^2 - n_2^2} (n_1^2 a \cos^2 \theta_1 + n_2^2 b \cos^2 \theta_2). \quad (\text{A14})$$

TM polarization:

$$R(\theta) = 1 - 4 \frac{n_c}{n_{ext}} \frac{\cos \theta}{\cos \theta_c} \left(\frac{n_2 \cos \theta_1}{n_1 \cos \theta_2} \right)^{2N}, \quad (\text{A15})$$

$$\omega_s(\theta) = \frac{\pi c}{2(n_1^2 a + n_2^2 b)} \frac{n_1 \cos \theta_2 + n_2 \cos \theta_1}{\cos \theta_1 \cos \theta_2}, \quad (\text{A16})$$

$$L_{\text{DBR}}(\theta) = \frac{2 \cos^2 \theta_1 \cos^2 \theta_2 (n_1^2 a + n_2^2 b)}{\cos^2 \theta_c (n_1^2 \cos^2 \theta_2 - n_2^2 \cos^2 \theta_1)}. \quad (\text{A17})$$

Appendix B: Asymmetric cavity, coupled cavity linewidth

In this Appendix we extend the treatment of Sec. 4.1 by deriving formulas for mode frequency and width of an asymmetric cavity, and also prove the results reported in Sec. 5.1 for a coupled cavity.

The dispersion equation for an asymmetric cavity of width L_c surrounded by mirrors with reflection coefficients r, r_c is

$$r r_c e^{2ik_c L_c} = 1. \quad (\text{B1})$$

This formula can be derived either by working out the transfer matrix of the structure using parametrizations (3), (4) for right and left mirrors, or by taking Eq. (11) for a cavity of width $2L_c$ in the limit $t_c \rightarrow 0$ for the central object. Introducing the usual parametrization (10) for the DBR reflection coefficient, this equation for ω can be solved in the complex plane yielding $\omega = \omega_m(\theta) - i\gamma_m(\theta)$, with the mode frequency given by

$$\omega_m = \frac{L_c \omega_c + \frac{1}{2}(L_{\text{DBR}} \omega_s + L_{\text{DBR},c} \omega_{s,c})}{L_c + \frac{1}{2}(L_{\text{DBR}} + L_{\text{DBR},c})} \quad (\text{B2})$$

and the mode halfwidth

$$\gamma_m = -\frac{c \ln \sqrt{R R_c}}{2n_c L_{\text{eff}} \cos \theta_c}, \quad (\text{B3})$$

where $L_{\text{eff}} = L_c + (1/2)(L_{\text{DBR}} + L_{\text{DBR},c})$, with obvious notations for the centers of stop bands and penetration depths. For $R, R_c \rightarrow 1$, formula (B2) reduces to Eq. (14) for the mode halfwidth of a symmetric cavity.

We now consider a symmetric structure with two cavities of width L_c coupled by a central mirror; the dispersion

equation is (11) of the main text. Since the central mirror is assumed to be symmetric, its reflection and transmission coefficients satisfy $t_c/t_c^* = -r_c/r_c^*$ (see Sec. 3). This implies that the phase of t_c differs from the phase of r_c by $\pm\pi/2$, or $t_c = \pm i r_c \sqrt{(1-R_c)/R_c}$. The \pm sign corresponds to an even or odd number of periods in the central mirror. The dispersion equation (11) can therefore be written as

$$r r_c e^{2ik_c L_c} = \frac{1}{1 \pm i \sqrt{\frac{1-R_c}{R_c}}}, \quad (\text{B4})$$

where the l.h.s. equals unity at the eigenfrequency of each isolated cavity (see Eq. (B1)). By expressing the l.h.s. in terms of the isolated cavity frequency (B2), (B3), the complex solutions for the coupled cavity are found as

$$\omega = \omega_m - i\gamma_m + \frac{ic \ln(1 \pm i \sqrt{\frac{1-R_c}{R_c}})}{2n_c L_{\text{eff}} \cos \theta_c}. \quad (\text{B5})$$

The imaginary part of the logarithm yields the optical splitting between S and A modes, while the real part gives a correction to the single cavity linewidth. We obtain:

$$\omega = \omega_m \pm V_{\text{opt}} - i\tilde{\gamma}_m, \quad (\text{B6})$$

where

$$V_{\text{opt}} = \frac{c}{2n_c L_{\text{eff}} \cos \theta_c} \arcsin \sqrt{1-R_c}, \quad (\text{B7})$$

$$\tilde{\gamma}_m = -\frac{c}{2n_c L_{\text{eff}} \cos \theta_c} \ln \sqrt{R}. \quad (\text{B8})$$

The expression for the optical coupling reduces for $R_c \rightarrow 1$ to Eq. (27) of the main text. The halfwidth is reduced compared to Eq. (B3) for a single cavity: the effect of optical coupling between the two cavities is to suppress the contribution to the linewidth coming from decay through the mirror of reflectivity R_c , and to leave only the decay rate through the external mirror of reflectivity R .

This conclusion can also be derived using the concept of *quasi-modes* [28], which are formed by the stationary states of a closed cavity weakly coupled to the external electromagnetic field. For a single cavity, the linewidth can be written as $\gamma_m = \gamma_{\text{left}} + \gamma_{\text{right}}$ in terms of the decay rates from either side; for a coupled cavity, since the eigenmodes S and A are linear combinations of single cavity modes, the matrix elements to left and right outer states are reduced by a factor $1/\sqrt{2}$, and the whole width is reduced by a factor of two.

Список литературы

- [1] J.J. Hopfield. Phys. Rev. **112**, 1555 (1958); V.M. Agranovich, J. Exptl. Theoret. Phys. **37**, 430 (1959); [Sov. Phys. JETP **37**, 307 (1960)].
- [2] C. Weisbuch, M. Nishioka, A. Ishikawa, Y. Arakawa. Phys. Rev. Lett. **69**, 3314 (1992).
- [3] R. Houdré, C. Weisbuch, R.P. Stanley, U. Oesterle, P. Pellandini, M. Illegems. Phys. Rev. Lett. **73**, 2043 (1994).

- [4] R. Houdré, R.P. Stanley, U. Oesterle, M. Ilegems, C. Weisbuch. *Phys. Rev.* **B49**, 16 761 (1994); T.R. Nelson, Jr., J.P. Prineas, G. Khitrova, H.M. Gibbs, J.D. Berger, E.K. Lindmark, J.-H. Shin, H.-E. Shin, Y.-H. Lee, P. Tayebati, L. Javniskis. *Appl. Phys. Lett.* **69**, 3031 (1996); L.A. Graham, Q. Deng, D.G. Deppe, D.L. Huffaker. *Appl. Phys. Lett.* **70**, 814 (1997).
- [5] T.B. Norris, J.K. Rhee, C.Y. Sung, Y. Arakawa, M. Nishioka, C. Weisbuch, *Phys. Rev.* **B50**, 14 663 (1994); H. Wang, J. Shah, T.C. Damen, W.Y. Jan, J.E. Cunningham, M. Hong, J.P. Mannaerts. *Phys. Rev.* **B51**, 14 713 (1995); G. Bongiovanni, A. Mura, F. Quochi, S. Gürtler, G.L. Staehli, F. Tassone, R.P. Stanley, U. Oesterle, R. Houdré. *Phys. Rev.* **B55**, 7084 (1997).
- [6] T.A. Fisher, A.M. Afshar, D.M. Whittaker, M.S. Skolnick, J.S. Roberts, G. Hill, A. Pate. *Phys. Rev.* **B51**, 2600 (1995).
- [7] J. Tignon, P. Voisin, C. Delalande, M. Voos, R. Houdré, U. Oesterle, R.P. Stanley. *Phys. Rev. Lett.* **74**, 3967 (1995); J. Tignon, R. Ferreira, J. Wainstain, C. Delalande, P. Voisin, M. Voos, R. Houdré, U. Oesterle, R.P. Stanley. *Phys. Rev.* **B56**, 4068 (1997).
- [8] T.A. Fisher, A.M. Afshar, M.S. Skolnick, D.M. Whittaker, J.S. Roberts. *Phys. Rev.* **B53**, R10469 (1996).
- [9] J.D. Berger, O. Lyngnes, H.M. Gibbs, G. Khitrova, T.R. Nelson, E.K. Lindmark, A.V. Kavokin, M.A. Kaliteevskii, V.V. Zapasskii. *Phys. Rev.* **B54**, 1975 (1996).
- [10] A. Armitage, T.A. Fisher, M.S. Skolnick, D.M. Whittaker, P. Kinsler, J.S. Roberts. *Phys. Rev.* **B55**, 16 395 (1997).
- [11] J.-K. Rhee, D.S. Citrin, T.B. Norris, Y. Arakawa, M. Nishioka. *Solid. State Commun.* **97**, 941 (1996); R. Houdré, J.L. Gibernon, P. Pellandini, R.P. Stanley, U. Oesterle, C. Weisbuch, J. O'Gorman, B. Roycroft, M. Ilegems. *Phys. Rev.* **B52**, 7810 (1995); F. Jahnke, M. Kira, S.W. Koch, G. Khitrova, E.K. Lindmark, T.R. Nelson, Jr., D.V. Wick, J.D. Berger, O. Lyngnes, H.M. Gibbs, K. Tai. *Phys. Rev. Lett.* **77**, 5257 (1996); O. Lyngnes, J.D. Berger, J.P. Prineas, S. Park, G. Khitrova, H.M. Gibbs, F. Jahnke, M. Kira, S.W. Koch, *Solid. State Commun.* **104**, 297 (1997).
- [12] R.P. Stanley, R. Houdré, C. Weisbuch, U. Oesterle, M. Ilegems. *Phys. Rev.* **B53**, 10 995 (1996); R.P. Stanley, S. Pau, U. Oesterle, R. Houdré, M. Ilegems. *Phys. Rev.* **B55**, 4867 (1997).
- [13] V. Savona, C. Weisbuch. *Phys. Rev.* **B54**, 10 835 (1996).
- [14] F. Tassone, C. Piermarocchi, V. Savona, A. Quattropani, P. Schwendimann. *Phys. Rev.* **B53**, R7642 (1996).
- [15] S. Pau, G. Björk, J. Jacobson, H. Cao, Y. Yamamoto. *Phys. Rev.* **B51**, 7090 (1995); S. Pau, G. Björk, H. Cao, F. Tassone, R. Huang, Y. Yamamoto, R.P. Stanley. *Phys. Rev.* **B55**, 1942 (1997).
- [16] D.M. Whittaker, P. Kinsler, T.A. Fisher, M.S. Skolnick, A. Armitage, A.M. Afshar, M.D. Sturge, J.S. Roberts. *Phys. Rev. Lett.* **77**, 4792 (1996); P. Kinsler, D.M. Whittaker. *Phys. Rev.* **B54**, 4988 (1996).
- [17] V. Savona, C. Piermarocchi, A. Quattropani, F. Tassone, P. Schwendimann. *Phys. Rev. Lett.* **78**, 4470 (1997).
- [18] A.V. Kavokin. *Phys. Rev.* **B57**, 3757 (1998).
- [19] D.M. Whittaker. *Phys. Rev. Lett.* **80**, 4791 (1998).
- [20] C. Ell, J. Prineas, T.R. Nelson, Jr., S. Park, H.M. Gibbs, G. Khitrova, S.W. Koch, R. Houdré, *Phys. Rev. Lett.* **80**, 4795 (1998).
- [21] J.J. Baumberg, A. Armitage, M.S. Skolnick, J.S. Roberts, *Phys. Rev. Lett.* **81**, 661 (1998).
- [22] G.R. Hayes, S. Haacke, M. Kauer, R.P. Stanley, R. Houdré, U. Oesterle, B. Deveaud. *Phys. Rev.* **B58**, 10 175 (1998).
- [23] F. Quochi, G. Bongiovanni, A. Mura, J.L. Staehli, B. Deveaud, R.P. Stanley, U. Oesterle, R. Houdré. *Phys. Rev. Lett.* **80**, 4733 (1998).
- [24] P. Kelkar, V. Kozlov, H. Leon, A. Nurmikko, C. Chu, D. Grillo, J. Han, C. Hua, R. Gunshor. *Phys. Rev.* **B52**, 5491 (1995).
- [25] L.S. Dang, D. Heger, R. André, F. Boeuf, A. Romestain. *Phys. Rev. Lett.* **81**, 3920 (1998).
- [26] T. Ishihara, T. Kuitani, Y. Sato, T. Fujita, M. Yamanishi. In: *Physics of Semiconductors* / Ed. by M. Scheffler and R. Zimmermann (World Scientific, Singapore, 1996), p. 3087; T. Fujita, Y. Sato, T. Kuitani, T. Ishihara. *Phys. Rev.* **B57**, 12 428 (1998).
- [27] D.G. Lidzey, D.D.C. Bradley, M.S. Skolnick, T. Virgili, S. Walker, D.M. Whittaker. *Nature* **395**, 53 (1998).
- [28] V. Savona, C. Piermarocchi, A. Quattropani, P. Schwendimann, F. Tassone. In: *New Aspects in Optical Properties of Nanostructures*, Special issue of Phase Transitions. Vol. **68** (Gordon and Breach, 1999).
- [29] G. Khitrova, H.M. Gibbs, F. Jahnke, M. Kira, S.W. Koch (to be published).
- [30] M.S. Skolnick, T.A. Fisher, D.M. Whittaker. *Semicond. Sci. Technol.* **13**, 645 (1998).
- [31] R.P. Stanley, R. Houdré, U. Oesterle, M. Ilegems, C. Weisbuch. *Appl. Phys. Lett.* **65**, 2093 (1994).
- [32] P. Pellandini, R.P. Stanley, R. Houdré, U. Oesterle, M. Ilegems, C. Weisbuch. *Appl. Phys. Lett.* **71**, 864 (1997).
- [33] A. Armitage, M.S. Skolnick, V.N. Astratov, D.M. Whittaker, G. Panzarini, L.C. Andreani, T.A. Fisher, J.S. Roberts, A.V. Kavokin, M.A. Kaliteevskii, M.R. Vladimirova. *Phys. Rev.* **B57**, 14877 (1998); G. Panzarini, L.C. Andreani, A. Armitage, D. Baxter, M.S. Skolnick, V.N. Astratov, J.S. Roberts, A.V. Kavokin, M.R. Vladimirova, M.A. Kaliteevskii. To be published in *Phys. Rev.* **B59**, (1999).
- [34] D.S. Citrin. *Phys. Rev.* **B49**, 1943 (1994); L.C. Andreani. *Phys. Stat. Sol. (b)* **188**, 29 (1995).
- [35] G. Panzarini, L.C. Andreani. *Phys. Rev.* **B52**, 10 780 (1995).
- [36] L. Pavesi, G. Panzarini, L.C. Andreani. *Phys. Rev.* **B58**, 15 798 (1998).
- [37] D.I. Babic, S.W. Corzine, *IEEE J. Quantum Electron.* **28**, 514 (1992).
- [38] V. Savona, L.C. Andreani, P. Schwendimann, A. Quattropani. *Solid State Commun.* **93**, 733 (1995).
- [39] A.V. Kavokin, M.A. Kaliteevskii. *Solid State Commun.* **95**, 859 (1995).
- [40] E.L. Ivchenko, M.A. Kaliteevskii, A.V. Kavokin, A.I. Nesvizhskii. *J. Opt. Soc. Am.* **B13**, 1061 (1996).
- [41] D. Baxter, M.S. Skolnick, A. Armitage, V.N. Astratov, D.M. Whittaker, T.A. Fisher, J.S. Roberts, D.J. Mowbray, M.A. Kaliteevskii. *Phys. Rev.* **B56**, R10032 (1997).
- [42] For a review see e.g. L.C. Andreani. In: *Confined Excitons and Photons: New Physics and Devices* / Ed. by E. Burstein and C. Weisbuch (Plenum, New York, 1995), p. 57.
- [43] E.L. Ivchenko, S. Jorda, A.I. Nesvizhskii. *Fiz. Tekn. Poluprov. (St-Petersburg)* **27**, 977 (1993); [*Sov. Phys. Semicond.* **27**, 530 (1993)].
- [44] D.S. Citrin. *Phys. Rev.* **B50**, 5497 (1994).
- [45] L.C. Andreani. *Phys. Lett.* **A192**, 99 (1994).
- [46] F. Tassone, F. Bassani, L.C. Andreani. *Il Nuovo Cimento* **D12**, 1673 (1990); F. Tassone, L.C. Andreani, F. Bassani. *Phys. Rev.* **B45**, 6023 (1992).
- [47] L.C. Andreani, F. Tassone, F. Bassani. *Solid State Commun.* **77**, 641 (1991).

- [48] E.L. Ivchenko. *Fiz. Tverd. Tela* **33**, 2388 (1991) [*Sov. Phys. Solid State* **33**, 1344 (1991)].
- [49] D.S. Citrin. *Phys. Rev.* **B47**, 3832 (1993).
- [50] M. Born, E. Wolf. *Principles of Optics*, 4th ed. Pergamon, N. Y. (1970).
- [51] H.A. McLeod. *Thin-Film Optical Filters*, 2nd ed. Hilger (1986).
- [52] A. Yariv, P. Yeh. *Optical Waves in Crystals* [5 Wiley, New York, (1984)].
- [53] C.R. Pidgeon, S.D. Smith. *J. Opt. Soc. Am.* **54**, 1459 (1964).
- [54] S. Jorda. *Phys. Rev.* **B51**, 10 185 (1995).
- [55] This approximate formula for the dispersion is usually derived from the relation $\omega_m = (c/n_{\text{eff}})\sqrt{k_z^2 + k_{\parallel}^2}$, considering that the wavevector along the cavity axis is quantized, leading to $\omega_m(\theta) = \omega_m(0)(1 - \sin^2 \theta/n_{\text{eff}}^2)^{-1/2}$.
- [56] H. Yokoyama, Y. Nambu, T. Kawakami. In: *Confined Excitons and Photons: New Physics and Devices* / Ed. by E. Burstein and C. Weisbuch (Plenum, New York, 1995), p. 427; G. Björk, Y. Yamamoto, H. Heitmann, *ibid.*, p. 467.
- [57] D.S. Citrin. *Solid State Commun.* **89**, 139 (1994).
- [58] L.C. Andreani. *Phys. Stat. Solidi (b)* **188**, 29 (1995).
- [59] G. Björk, S. Pau, J.M. Jacobson, H. Cao, Y. Yamamoto. *Phys. Rev.* **B52**, 17 310 (1995).
- [60] V.M. Agranovich, G.C. La Rocca, F. Bassani. *Phys. Stat. Sol. (a)* **164** 39 (1997); G.C. La Rocca, F. Bassani, V.M. Agranovich. *J. Opt. Soc. Am.* **B15**, 652 (1998).
- [61] V.M. Agranovich, H. Benisty, C. Weisbuch. *Solid State Commun.* **102** 631 (1997).
- [62] This sample was first reported in T.A. Fisher, A.M. Afshar, M.S. Skolnick, D.M. Whittaker, J.S. Roberts, *Solid State Electron.* **40**, 493 (1996) and in Ref. 8.
- [63] The more precise values quoted in Ref. 41 include absorption, as well as oxidation of the top 50 Å of the top AlGaAs layer.
- [64] Experimentally, another reason for the dominant TM polarization is that the reflection coefficient of the cryostat window is greater for TE than for TM, therefore the intensity of light falling on the sample is larger for TM than for TE.
- [65] J.T. Boyd. *IEEE J. Quantum Electr.* **8**, 788 (1972).
- [66] R. Atanasov, F. Bassani, A. D'Andrea, N. Tomassini. *Phys. Rev.* **B50**, 14 381 (1994); R.C. Iotti, L.C. Andreani. *Phys. Rev.* **B56**, 3922 (1997).
- [67] I. Carusotto, G.C. La Rocca. *Phys. Stat. Sol. (a)* **164**, 377 (1997).
- [68] G. Panzarini (unpublished).
- [69] W.T. Masselink, P.J. Pearah, J. Klem, C.K. Peng, H. Morkoç, G.D. Sanders, Y.-C. Chang. *Phys. Rev.* **B32**, 8027 (1985).
- [70] S. Frisk, J.-L. Staehli, L.C. Andreani, A. Bosacchi, S. Franchi. In: *Optics of Excitons in Confined Systems* / Ed. by A. D'Andrea, R. Del Sole, R. Girlanda, and A. Quattropani (IOP Conference Series **123**), p. 183 (1992).
- [71] L.C. Andreani, G. Panzarini, A.V. Kavokin M.R. Vladimirova. *Phys. Rev.* **B57**, 4670 (1998).